Gyroless satellite attitude determination using a SVD-Laplace Particle Filter

Karim Dahia, Nadjim Horri, Christian Musso, Nicolas Merlinge

Gyroless satellite attitude determination using a SVD-Laplace Particle Filter

Karim Dahia[1], Nadjim Horri[2], Christian Musso[1] and Nicolas Merlinge[1]

[1] *ONERA - The French Aerospace Lab, 6 Chemin de la Vauve aux Granges, 91123 Palaiseau, France. Email: karim.dahia@onera.fr, christian.musso@onera.fr, nicolas.merlinge@onera.fr*

[2] *School of Future Transport Engineering, Faculty of Engineering and Computing Coventry University, CV1 5FB, United Kingdom. Email: nadjim.horri@coventry.ac.uk*

Abstract

There is an increasing demand in the space industry for methods allowing for gyroless spacecraft attitude determination to either provide low cost sensor fusion or to recover from gyro failures. The gyroless configuration used in this paper is a combination of magnetometers and Sun sensors. Sun sensors are subject to measurement discontinuities during solar eclipses. Gyroless attitude sensing is known to increase sensitivity to measurement noise and model uncertainty. This paper presents a new Laplace Particle Filter with a Singular Value Decomposition to enhance attitude determination performance under these circumstances, while also preventing filter degeneracy. An orthogonal Procrustes problem is formulated to minimise the Wahba cost function and determine the attitude matrix from the Sun and magnetic field vectors and a third virtual predicted measurement vector, which is also available during Sun occlusion. The proposed filter is compared to a regularised particle filter approach, which handles particle filter degeneracy. Both filters are applied to the attitude determination of a small Earth observation satellite using three Sun sensors available during the sunlit phase and three orthogonal magnetometers. A Monte Carlo numerical simulation analysis demonstrates that the proposed particle filter significantly outperforms the regularised particle filter in terms of accuracy and robustness to the Sun sensor measurement discontinuities during solar eclipse and is also more accurate when both types of sensor measurements are available.

Keywords: Particle filter, Satellite, Attitude determination, SVD, Sun sensor, Magnetometer, Gyroless, Procrustes problem.

1. Introduction

Satellite Attitude Determination Systems (ADS) are crucial for space missions. Their development presents challenges when the number of onboard sensors and the accuracy are limited for cost or spacecraft design considerations,

especially in the case of small satellites and cubesats. Kalman filtering has successfully been applied for a wide range of applications and is commonly used for satellite attitude determination. It is the optimal maximum likelihood estimator under the assumption of a linear system model, with Gaussian assumptions on measurement and process noise. The extension of Kalman filtering to nonlinear systems, known as the extended Kalman filter (EKF), often represents a sensible suboptimal solution for satellite attitude determination [1, 2]. The unscented Kalman filter (UKF) improves estimation performance in systems with nonlinearities by deterministically generating a number of *sigma-points* to approximate a Gaussian distribution under non-linear transformations and its higher order moments. The UKF was also applied to satellite attitude determination [3]. The EKF and UKF can however lose robustness and accuracy or even stability in the presence of high initial uncertainty, coarse sensing, strong nonlinearities, sensor faults or measurement discontinuities as in the case of solar eclipses.

The application under consideration in this paper is satellite ADS with Sun sensors and magnetometers. Sun sensors measurements are unavailable during solar eclipse and magnetometers continuously measure the Earth's magnetic field, which exhibits a different behaviour in polar regions. Unintended gaps between sensors measurements may also be caused by sensor faults. Gyro faults and failures have often caused a faulty attitude determination and even mission loss, as in the case of the Worldview-4 satellite lost by Digitalglobe in 2019. There is consequently an increased interest for methods allowing for gyroless attitude determination to deal with such failures or to provide a lower cost satellite attitude determination in small satellites. These methods often employ the remaining attitude determination sensors using EKF or UKF filters, which are sometimes combined with vector based observation methods such as Davenport's q-method, the quaternion estimator (QUEST) and the singular value decomposition (SVD) [4]. By measuring vectors such as the Sun and magnetic field vectors in a body frame and modelling them in the Earth centred inertial frame, it is possible to determine a rotation matrix between the two frames by solving the so-called Wahba's problem. A minimum of two vector observations is however necessary to provide an indirect attitude measurement to the attitude determination algorithms and solve this problem. Gyroless attitude determination however suffers from a higher sensitivity to measurement noise and model uncertainty [5]. It can also be convenient to reformulate Wahba's problem as an orthogonal Procrustes problem that determines the orthogonal transformation between matrices instead of vectors. The Procrustes problem was indeed used to recast Wahba's problem as a linear matrix inequality (LMI) problem in [6] and applied to spacecraft attitude determination from ellipsoid observations in [7].

With few exceptions such as [8], little research was focused on exploiting the strengths of vector-based observations and non-linear estimation methods to preserve maximum likelihood optimality in the non-linear case, especially in the case of sensor faults or measurement discontinuities. Nonlinear estimation approaches to satellite attitude determination have included orthogonal filters

based on propagating rotation matrices rather than attitude quaternions or Euler angle, predictive filters where the output is linearised rather than the state, observers where a prediction model is assumed and the estimation may be sub-optimal but stable for a range of initial conditions, adaptive filters where the estimator updates noise covariances [9] or Particle Filters [10]. Particle Filters can be viewed as a discrete approximation to the optimal filter for such non-linear systems even in the case of multimodalities. This is done by sampling a set of weighted admissible states called particles. Particles are propagated according to the dynamics and their weights are recursively modified using measurement updates. When the weights distribution degenerates, the particles can be re-sampled in a new particle set, closer to the solution. Different strategies have been developed for the state and measurement updates and for particle filter resampling. Examples of particle filters include the Bootstrap/Monte Carlo filter in [10, 11, 12], the regularised particle filter (RPF [13]), the box particle filter [14, 15] and the Laplace Particle Filter (LPF [16]). The LPF is currently one of the most robust and accurate particle filtering approaches because it relies on a suitable formulation of the proposal density. The key idea lies in the resampling step, where particles are sampled according to an optimal proposal density (or importance function) whose expectancy corresponds to the *Maximum A Posteriori* (MAP). The choice of the proposal density depends on the problem formulation and must be handled carefully. The LPF was applied to target tracking [17, 18] and non-linear and ambiguous terrain navigation [19]. For gyroless attitude determination, an unscented particle filter was also developed using the UKF to generate the proposal distribution of the particle filter, with improved accuracy compared to the UKF [20]. However, the results presented in that paper appear to only demonstrate convergence from low initial uncertainties on the attitude about a single axis and using highly accurate star sensing. From a practical implementation viewpoint, particle filtering is often associated with high computational demand, when a large number of particles is needed, especially in high dimensional or highly non-linear system modes. The relatively higher computational demand of particle filters is increasingly being addressed in the aerospace field by new computational solutions such as onboard graphics processing unit (GPU) applications [21, 22].

In this paper, a LPF is combined with a singular value decomposition (SVD) for gyroless attitude determination on all three axes for a small Earth observation satellite using a combination of three magnetometers and three Sun sensors. More precisely, three orthogonal Sun sensors out of six are lit by the Sun during the sunlit phase, which is a standard configuration [2]. This combination of sensors is considered because most satellites rely on them in at least one of their attitude determination and control system (ADCS) modes. With this configuration, both sensor types are used except during the solar eclipse when Sun sensors become unavailable.

The main contributions of the paper are:

- A new LPF for which the proposal density is designed using a SVD for gyroless satellite attitude determination. The approach is used to enhance

accuracy and robustness to measurement discontinuities and to efficiently prevent filter degeneracy,

- The SVD is used to solve a maximum a posteriori (MAP) Procrustes problem for gyroless attitude determination. This is done by converting Sun sensor, magnetometer and a third orthogonal virtual *a priori* vector measurement to provide indirect attitude measurement inputs to the filter. During the solar eclipse, the calculation of the virtual *a priori* vector crucially maintains uninterrupted gyroless attitude determination with magnetometer measurements alone.

The SVD-LPF is compared to a classical RPF in terms of attitude determination accuracy and robustness. The comparison is focussed on particle filtering methods for paper length considerations and because the limitations of the sub-optimal EKF and UKF for non-linear problems with severe uncertainty, measurement discontinuities, coarse sensing in small satellites or faults are already known from the existing literature [23] and adaptive formulations of these approaches are generally focused on addressing one of those issues as in [5] where the focus is on sensor faults. The SVD-LPF and RPF are compared under two scenarios, respectively with moderate and high magnetometer accuracies when the satellite is in the Earth's shadow, which occurs during approximately one third of the orbit. Increased attitude determination accuracy is possible when the satellite is not in eclipse because the Sun sensors are then also available. The SVD-LPF is shown to outperform the RPF in terms of state estimation accuracy when both sensor types are available. The improvement in attitude determination accuracy is even more significant during eclipse, with enhanced robustness to measurement discontinuities.

The paper is organised as follows. Section 2 describes the mathematical model of satellite attitude dynamics and kinematics and the measurement models. Section 3 describes optimal non-linear filtering problem and the Particle filtering approach. The SVD-Laplace Particle Filter approach is then presented in Section 4. In Section 5, a comparative Monte Carlo numerical simulation analysis is presented between the SVD-LPF and the RPF for satellite attitude determination accuracy and robustness with a discussion of real time implementation considerations. Finally, Section 6 concludes the paper.

2. Motion and Measurement Models

2.1. Dynamic and kinematic models

If no external disturbance torque is assumed, the dynamic model of a rigid body satellite is given by Euler's rotational equation of motion:

$$\dot{\mathbf{L}} + \boldsymbol{\omega} \times \mathbf{L} = 0, \tag{1}$$

where $\times$ denotes the cross product, $\mathbf{L}$ denotes the total angular momentum and $\boldsymbol{\omega} = [\omega_1, \omega_2, \omega_3]^T$ is the angular velocity vector, both in the body fixed reference frame.

The equation of the total angular momentum is:

$$\mathbf{L} = \mathbf{I}\boldsymbol{\omega}. \tag{2}$$

By substituting $\mathbf{L}$ from equation (2), into the equation (1), we obtain the general Euler's rotational equation using three orthogonal reaction wheels on the body axes of the satellite:

$$\mathbf{I}\dot{\boldsymbol{\omega}} = -\boldsymbol{\omega} \times \mathbf{I}\boldsymbol{\omega} + \mathbf{u} + \mathbf{w}, \tag{3}$$

where $\mathbf{I}$ is the moment of inertia matrix of the body of the satellite about its centre of mass.
The control torque of the wheels on the satellite is defined as:

$$\mathbf{u} = -\dot{\mathbf{h}} + \boldsymbol{\omega} \times \mathbf{h}, \tag{4}$$

where $\mathbf{h}$ is the momentum of the wheels. For simplicity, the wheels will typically operate in a conventional zero momentum mode. The vector $\mathbf{w}$ represents the angular velocity components of the white process noise that verifies the following properties:

$$\mathbb{E}[\mathbf{w}] = 0, \tag{5a}$$

$$\mathbb{E}\left[\mathbf{w}\mathbf{w}^{\mathbf{T}}\right] = \mathbf{Q}, \tag{5b}$$

where $\mathbb{E}$ denotes expectation.

Using the quaternion representation of attitude kinematics, the kinematic model of a satellite is given by:

$$\begin{cases} \dot{\bar{\mathbf{q}}} = -\frac{1}{2}\boldsymbol{\omega_o} \times \bar{\mathbf{q}} + \frac{1}{2} q_0 \boldsymbol{\omega_o}, \\ \dot{q}_0 = -\frac{1}{2}\boldsymbol{\omega_o}^T \bar{\mathbf{q}}, \end{cases} \tag{6}$$

where $\mathbf{q} = \left[q_0, \bar{\mathbf{q}}^T\right]^T = [q_0, q_1, q_2, q_3]^T$ is the attitude quaternion of the satellite with respect to the local orbit frame, q_0 and $\bar{\mathbf{q}}$ respectively represent the scalar and vector parts of the quaternion and the angular velocity with respect to the local orbit frame $\boldsymbol{\omega_o} = \boldsymbol{\omega} - \mathbf{R_o^b}\,[0, -n, 0]^T$, where n is the mean orbital rate. The attitude quaternion satisfies the following equation:

$$q_0^2 + q_1^2 + q_2^2 + q_3^2 = 1. \tag{7}$$

The rotation matrix $\mathbf{R_o^b}$ from the local orbit frame to the body frame is given by:

$$\mathbf{R}_o^b = \begin{pmatrix} q_0^2 + q_1^2 - q_2^2 - q_3^2 & 2\left(q_1 q_2 - q_0 q_3\right) & 2\left(q_0 q_2 + q_1 q_3\right) \\ 2\left(q_0 q_3 + q_1 q_2\right) & q_0^2 - q_1^2 + q_2^2 - q_3^2 & 2\left(q_2 q_3 - q_0 q_1\right) \\ 2\left(q_1 q_3 - q_0 q_2\right) & 2\left(q_0 q_1 + q_2 q_3\right) & q_0^2 - q_1^2 - q_2^2 + q_3^2 \end{pmatrix}. \tag{8}$$

For the sake of convenience, the dynamic and kinematic models are written in the form of an affine control system:

$$\dot{\mathbf{x}} = F(\mathbf{x}) + \mathbf{G}\mathbf{u} + \mathbf{D}\mathbf{w}, \tag{9}$$

where $\mathbf{x} = \left[\mathbf{q}^T, \boldsymbol{\omega}^T\right]^T \in \mathbb{R}^7$ is the state vector and $\mathbf{u} \in \mathbb{R}^3$ was previously defined.

The dynamical model $F(\mathbf{x})$, the control input matrix $\mathbf{G}$ and the process noise input matrix $\mathbf{D}$ are respectively given by:

$$F(\mathbf{x}) = \left[\dot{\mathbf{q}}^T, \dot{\boldsymbol{\omega}}^T\right]^T_{\substack{\mathbf{u}=0_{3\times 1} \\ \mathbf{w}=0_{3\times 1}}} : \mathbb{R}^7 \to \mathbb{R}^7, \tag{10}$$

$$\mathbf{G} = \begin{bmatrix} \mathbf{0}_{4\times 3} \\ \mathbf{I}^{-1} \end{bmatrix} : \mathbb{R}^7 \to \mathbb{R}^{7\times 3}, \tag{11}$$

$$\mathbf{D} = \begin{bmatrix} \mathbf{0}_{4\times 3} \\ \mathbf{I}_d \end{bmatrix} : \mathbb{R}^7 \to \mathbb{R}^{7\times 3}, \tag{12}$$

where $\mathbf{I}_d$ is the 3×3 identity matrix.

This mathematical model of attitude kinematics and dynamics will be used for the simulation analysis of all attitude determination algorithms.

Without loss of generality, the mathematical model of equation (9) is taken to be in a zero momentum normal operation mode in the remainder of the paper, implying that $\mathbf{u} = \mathbf{0}$, which is a common assumption in estimation performance analysis. All external disturbances are neglected for simplicity.

2.2. Measurement models

The Sun vector is first modelled in the Earth centred inertial (ECI) frame, using a Sun ephemeris function, which is available in the companion software of David Vallado's textbook on the fundamentals of astrodynamics and applications [24]. For a Julian date specified in days, that function returns the Sun position vector in ECI frame, as well as the right ascension and declination angles. Given the satellite position vector in ECI frame and the Sun position in ECI frame, it is then straightforward to compute the Sun vector from the satellite body frame to the Sun. The Sun sensor frame is obtained by a constant rotation sequence from the satellite body frame, which is assumed here to be the identity matrix for simplicity. The three components of the measured Sun vector in sensor frame are determined using the three orthogonal Sun sensors out of six that are lit by the Sun during the sunlit phase [2].

The Sun sensor vector observation equation is given by:

$$\mathbf{Y}_s = \mathbf{R}_o^b \mathbf{B}_s + \boldsymbol{\nu}_s, \tag{13}$$

where $\mathbf{Y}_s$ is the Sun vector in the satellites body frame, $\mathbf{R}_o^b$ is the rotation matrix from the local orbit frame to the body frame and $\mathbf{B}_s$ is the modelled Sun vector in the local orbit frame with:

$$\|\mathbf{B}_s\|^2 = 1, \tag{14}$$

and $\boldsymbol{\nu}_s$ is the Sun sensor noise with:

$$\boldsymbol{\nu}_s^T \left(\mathbf{R}_o^b \mathbf{B}_s\right) = 0. \tag{15}$$

Shuster and Oh [25] have shown that nearly all the distribution of the measurement errors is concentrated on a very small area about the direction of $\mathbf{R}_o^b \mathbf{B}_s$, so the sphere containing that point can be locally approximated by a tangent plane, characterized by the equation (13). The sensor noise $\boldsymbol{\nu}_s$ is approximately Gaussian and satisfies:

$$\mathbb{E}[\boldsymbol{\nu}_s] = 0, \tag{16a}$$

$$\Sigma_s \triangleq \mathbb{E}[\boldsymbol{\nu}_s \boldsymbol{\nu}_s^T] = \sigma_s^2 \left(\mathbf{I}_d - \left(\mathbf{R}_o^b \mathbf{B}_s\right) \left(\mathbf{R}_o^b \mathbf{B}_s\right)^T\right). \tag{16b}$$

Equation (16b) is known as the QUEST measurement covariance matrix [26, 27]. Note that equation (16b) is a function of the unknown true values in $\mathbf{R}_o^b$ as mentioned in [28]. The approximations in the covariance matrix are discussed in [29, 27]. The covariance matrix Σ_s is rank-deficient [30], which would appear to cause problems with filtering algorithms. However, Shuster also explains in [27] that the following simpler nonsingular matrix:

$$\Sigma_s = \sigma_s^2 \mathbf{I}_d, \tag{17}$$

yields equivalent results. The advantage of using the equation (17) is that it does not contain the unknown true values and that it has been extended to large field-of-wiews [28]. Note that equation (17) also remains valid for all attitude measurements that can be converted to unit vectors such as the three axes magnetometer, which will be presented in the next paragraph.

For numerical simulation purposes, the Earth's magnetic field vector $\mathbf{B}_m$ in the local orbit frame is modelled using a 10^{th} order International Geomagnetic Reference Field (IGRF) model that uses a spherical harmonic representation of the magnetic-potential function [24]. The Gaussian geomagnetic field coefficients used are valid for 2020-2025 and this model is updated every five years. An IGRF function was used to express the magnetic field vector as a function of longitude, latitude and altitude, for which the time evolutions were obtained by a Simplified General Perturbation (SGP4) orbit propagator function.

The observation equation for the magnetometer vector observation is given by:

$$\mathbf{Y}_m = \mathbf{R}_o^b \mathbf{B}_m + \boldsymbol{\nu}_m, \tag{18}$$

where $\mathbf{Y}_m$ is the measured magnetic field vector in the satellites body frame, $\mathbf{B}_m$ is the modelled magnetic field vector in the local orbit frame with:

$$\|\mathbf{B}_m\|^2 = 1, \tag{19}$$

and $\boldsymbol{\nu}_m$ is the magnetometer noise with:

$$\boldsymbol{\nu}_m^T \left(\mathbf{R}_o^b \mathbf{B}_s\right) = 0. \tag{20}$$

As in the case of the Sun sensor noise, the magnetometer noise $\boldsymbol{\nu}_m$ is also approximately Gaussian and satisfies:

$$\mathbb{E}[\boldsymbol{\nu}_m] = 0, \tag{21a}$$

$$\mathbb{E}[\boldsymbol{\nu}_m \boldsymbol{\nu}_m^T] = \sigma_m^2 \left(\mathbf{I}_d - \left(\mathbf{R}_o^b \mathbf{B}_m \right) \left(\mathbf{R}_o^b \mathbf{B}_m \right)^T \right). \tag{21b}$$

Again, as also explained in [27], the covariance matrix Σ_m can be approximated by:

$$\Sigma_m \triangleq \mathbb{E}[\boldsymbol{\nu}_m \boldsymbol{\nu}_m^T] = \sigma_m^2 \mathbf{I}_d. \tag{22}$$

For ease of notation, the attitude matrix $\mathbf{R} = \mathbf{R}_o^b$ is used for the remainder of this article. The notations $\mathbf{Y}_s$ and $\mathbf{B}_s$ are not standard for Sun vectors but will improve notation homogeneity in Section 4.

The observation function is given by:

$$H(\mathbf{x}) = \begin{cases} [\mathbf{R}\,\mathbf{B}_s, \mathbf{R}\,\mathbf{B}_m]^T : \mathbb{R}^7 \to \mathbb{R}^6, & \text{during the sunlit phase;} \\ \mathbf{R}\,\mathbf{B}_m : \mathbb{R}^7 \to \mathbb{R}^3, & \text{during the Sun occlusion.} \end{cases} \tag{23}$$

where $\mathbf{R} = \mathbf{R}(\mathbf{q})$ is given by equation (8).

For this representation of the problem under consideration, estimation of $\mathbf{x}$ requires non-linear filtering techniques. In the next section, optimal non-linear filtering is used for a non-linear model of satellite attitude dynamics.

3. The non-linear filtering

3.1. Bayesian Estimation and Particle Filtering

The non-linear dynamic system model can be written in discrete time as:

$$\begin{cases} \mathbf{x}_k = F_k(\mathbf{x}_{k-1}, \mathbf{u}_k) + \mathbf{w}_k, \\ \mathbf{y}_k = H_k(\mathbf{x}_k) + \mathbf{v}_k, \end{cases} \tag{24}$$

where $\mathbf{x}_k$ is the state vector of dimension n, $\mathbf{u}_k$ is the control input of dimension s, $\mathbf{y}_k$ is the observation vector of dimension m. For our application, the dimension n of the state vector is 7 and the dimension m of the observation vector is either 6 in the sunlit phase or 3 in the Sun occlusion phase. F_k and H_k are two continuously differentiable maps from $\mathbb{R}^n$ to $\mathbb{R}^n$ and from $\mathbb{R}^n$ to $\mathbb{R}^m$. F_k is obtained by discretisation of the continuous time dynamic model of equation (10) and H_k is obtained by discretisation of the observation function of equation (23), $\mathbf{w}_k$ and $\mathbf{v}_k$ denote the dynamic and observation noise vectors. The system model assumes additive noise, which is typical in satellite and other applications. It is also assumed that the distributions of $\mathbf{w}_k$ and $\mathbf{v}_k$ are Gaussian with zero mean (see equations (5a), (16a) and (21a)) and their covariance matrices are $\mathbf{Q}_k$ and $\mathbf{R}_k$, respectively. The initial state vector $\mathbf{x}_0$ is assumed to be random with a known distribution.

The optimal non-linear filtering requires the calculation of the posterior density of the state variables at each time given the past measurements. The simplified notation $\mathbf{y}_{1:k}$ will be used as a shorthand for $\mathbf{y}_1, \ldots, \mathbf{y}_k$. Let $p_k(\mathbf{x}_k|\mathbf{y}_{1:k})$ be the posterior density of $\mathbf{x}_k$ given the measurements $\mathbf{y}_{1:k}$ and $p(\mathbf{x}_k|\mathbf{y}_{1:k-1})$ be the prior density of $\mathbf{x}_k$ given the measurements $\mathbf{y}_{1:k-1}$. The filtering algorithm consists of two steps:

1. *The prediction step*: The prior density is computed via the Chapman-Kolmogorov equation:

$$p(\mathbf{x}_k|\mathbf{y}_{1:k-1}) = \int_{\mathbb{R}^n} p(\mathbf{x}_k|\mathbf{x}_{k-1}) p(\mathbf{x}_{k-1}|\mathbf{y}_{1:k-1}) d\mathbf{x}_{k-1}, \tag{25}$$

   where $p(\mathbf{x}_k|\mathbf{x}_{k-1})$ denotes the transition density and $p(\mathbf{x}_{k-1}|\mathbf{y}_{1:k-1})$ denotes the previous posterior density.
2. *The correction step*: The posterior density of the state is calculated via Bayes' law:

$$p(\mathbf{x}_k|\mathbf{y}_{1:k}) = \frac{p(\mathbf{x}_k|\mathbf{y}_{1:k-1}) p(\mathbf{y}_k|\mathbf{x}_k)}{\int p(\mathbf{x}_k|\mathbf{y}_{1:k-1}) p(\mathbf{y}_k|\mathbf{x}_k) d\mathbf{x}_k}, \tag{26}$$

   where $p(\mathbf{y}_k|\mathbf{x}_k)$ denotes the likelihood function.

In the sequel, we denote the likelihood function $g(\mathbf{x}_k)$ and the prior (or predicted) density $q(\mathbf{x}_k)$ as follows:

$$\begin{cases} g(\mathbf{x}_k) = p(\mathbf{y}_k|\mathbf{x}_k), \\ q(\mathbf{x}_k) = p(\mathbf{x}_k|\mathbf{y}_{1:k-1}). \end{cases} \tag{27}$$

The particle filter can be viewed as an approximation to the above optimal non-linear filter based on Monte-Carlo sampling to approximate the conditional or predictive distribution by a mixture of Dirac distribution. The Sampling Importance Resampling Particle Filter and the Laplace Particle Filter are described here in order to highlight the similarity between them and the SVD-Laplace Particle Filter.

3.2. Particle Filter (Sampling Importance Resampling)

Assume that at time $k-1$, one has an approximation to the filtering density $p(\mathbf{x}_{k-1}|\mathbf{y}_{1:k-1})$ of the form $\sum_{i=1}^{N} \omega_{k-1}^i \delta(\mathbf{x}_{k-1} - \mathbf{x}_{k-1}^i)$ where ω_{k-1}^i are positive weights summing to 1, $\mathbf{x}_{k-1}^1, \ldots, \mathbf{x}_{k-1}^N$ are points in $\mathbb{R}^n$ (called particles), $\delta(\mathbf{x}_{k-1} - \mathbf{x}_{k-1}^i)$ denotes the Dirac distribution located at $\mathbf{x}_{k-1}^i$ and N the number of particles. From equation (25), the prior density is approached by a mixture of Dirac distributions:

$$p(\mathbf{x}_k|\mathbf{y}_{1:k-1}) \approx \sum_{i=1}^{N} \omega_{k-1}^i \delta(\mathbf{x}_k - \mathbf{x}_k^i).$$

Then, from equation (26), the posterior density of $\mathbf{x}_k$ given $\mathbf{y}_{1:k}$ is again approached by a mixture of Dirac distributions:

$$p(\mathbf{x}_k|\mathbf{y}_{1:k}) \approx \sum_{i=1}^{N} \omega_k^i \delta(\mathbf{x}_k - \mathbf{x}_k^i). \tag{28}$$

with weights:

$$\omega_k^i = \frac{\omega_{k-1}^i g(\mathbf{x}_k^i)}{\sum_{j=1}^{N} \omega_{k-1}^j g(\mathbf{x}_k^j)}. \tag{29}$$

The main problem of the particle filter is the degeneracy phenomenon, where after several iterations, the largest weights are concentrated on a few particles. This phenomenon generally leads to divergence as the filter operates with too few particles. This occurs when there are few particles near the true system state, but since the particles evolve according to the system dynamics, which often diverge, this phenomenon cannot be avoided unless resampling is performed. Resampling consists of drawing new particles according to the distribution of the particles cloud and reassigning them with the same weights. Therefore, a resampling step is triggered when degeneracy is about to occur. The particle weights are monitored using the following criterion:

$$N_{eff} = \frac{1}{\sum_{i=1}^{N} (\omega^i)^2} < N_{th}. \tag{30}$$

A resampling step occurs when N_{eff} falls below a given threshold $N_{th} = \theta N$, where $\theta \in (0, 1)$ is an a priori defined parameter.

The following steps summarise the Sampling Importance Resampling algorithm with a prior density $p(\mathbf{x}_k|\mathbf{x}_{k-1})$ [10]:

1. **Initialisation**: sample $\mathbf{x}_0^i \sim p(\mathbf{x}_0)$ for $i = 1, \ldots, N$ and set $\omega_0^i = \frac{1}{N}$.
2. **Prediction**: sample $\mathbf{x}_k^i \sim p(\mathbf{x}_k|\mathbf{x}_{k-1}^i)$.
   for $i = 1, \ldots, N$
3. **Correction**:
   - compute the weights $\varpi_k^i = \omega_{k-1}^i g(\mathbf{x}_k^i)$,
   - set $\omega_k^i = \frac{\varpi_k^i}{\sum_{j=1}^{N} \varpi_k^j}$,
   - compute $\hat{\mathbf{x}}_k = \sum_{i=1}^{N} \omega_k^i \mathbf{x}_k^i$ and $\mathbf{P}_k = \sum_{i=1}^{N} \omega_k^i (\mathbf{x}_k^i - \hat{\mathbf{x}}_k)(\mathbf{x}_k^i - \hat{\mathbf{x}}_k)^T$.
4. **Resampling**: discard/multiply particles $\left\{\mathbf{x}_k^i\right\}_{i=1,\ldots,N}$ according to high/low weights ω_k^i.

This algorithm can be significantly improved when considering proposal densities which take into account the current measurement. In this case, the particles $\mathbf{x}_k^i$ are sampled according to a proposal density $\tilde{q}$ and the weights ω_k^i are calculated as follows:

$$\omega_k^i \propto \omega_{k-1}^i \frac{g(\mathbf{x}_k^i) q(\mathbf{x}_k^i)}{\tilde{q}(\mathbf{x}_k^i)}, \tag{31}$$

where $g(.)$ and $q(.)$ are defined in equation (27). In the next section, a proposal density based on Laplace approximation [18] is described.

3.3. The Laplace Particle Filter (LPF)

The choice of the proposal density $\tilde{q}$ is crucial for the control of the Monte Carlo error. The LPF [16, 17] operates in the same way as the particle filter except for the resampling stage. Indeed, the LPF resampling is based on an optimal proposal density $\tilde{q}$ centered on the MAP, which showed superior accuracy and robustness. The optimal proposal density is obtained for $\tilde{q}_{opt} = p(\mathbf{x}|\mathbf{y})$. For this purpose, LPF chooses a proposal density, which may be Gaussian with moments nearly equal to those of the posterior. The posterior expectation $\mathbb{E}[\mathbf{x}|\mathbf{y}]$ and the posterior covariance matrix $\mathbb{V}[\mathbf{x}|\mathbf{y}]$ are well approximated by the Laplace formula:

$$\begin{cases} \mathbb{E}[\mathbf{x}|\mathbf{y}] \approx \mathbf{x}^L = \mathbf{x}^* + \beta(\mathbf{x}^*, \mathbf{J}^*), \\ \mathbb{V}[\mathbf{x}|\mathbf{y}] \approx \mathbf{P}^L = (\mathbf{J}^*)^{-1} + \gamma(\mathbf{x}^*, \mathbf{J}^*), \end{cases} \tag{32}$$

where β, γ are two exact high-order corrective terms. The MAP, which is denoted $\mathbf{x}^*$ and the observed Fisher information matrix $\mathbf{J}^*$ are calculated by solving the following problem:

$$\begin{cases} \mathbf{x}^* = \arg\max_{\mathbf{x}} (g(\mathbf{x})\, q(\mathbf{x})), \\ \mathbf{J}^* = - \left. \dfrac{\partial^2 \, \log(g(\mathbf{x})\, q(\mathbf{x}))}{\partial \mathbf{x}^2} \right|_{\mathbf{x}=\mathbf{x}^*}. \end{cases} \tag{33}$$

The following approximation yields a suitable estimation accuracy:

$$\begin{cases} \mathbf{x}^L \approx \mathbf{x}^*, \\ \mathbf{P}^L \approx (\mathbf{J}^*)^{-1}. \end{cases} \tag{34}$$

The covariance matrix $(\mathbf{J}^*)^{-1}$ can be approximated by:

$$\mathbf{J}^* \approx - (\log g)'' (\mathbf{x}^*) + (\mathbf{P}^-)^{-1}, \tag{35}$$

where $\mathbf{P}^-$ is the prior covariance matrix. The matrix $(\mathbf{J}^*)^{-1}$ can be taken equal to the prior covariance matrix $\mathbf{P}^-$. The new sample is drawn according to the proposal density $\tilde{q}(\mathbf{x})$ given by:

$$\tilde{q}(\mathbf{x}) = \mathcal{N}(\mathbf{x}; \mathbf{x}^*, \mathbf{P}^-), \tag{36}$$

where $\mathcal{N}$ is the Gaussian probability density function with $\mathbf{x}^*$ mean and $\mathbf{P}^-$ covariance matrix.

4. The SVD-Laplace Particle Filter (SVD-LPF)

The SVD-LPF, which is the main contribution of the paper, is derived from the classical LPF (see Section 3.3) and adapted to the attitude determination problem using Sun and magnetic field vector measurements for which the models are defined in Section 2.

A maximum a posteriori (MAP) optimisation condition is calculated using the Procrustes problem. Two possible measurement configurations are considered:

- Case 1: Only the magnetic field is available (e.g. during sun occlusions case);
- Case 2: Magnetic field measurement $\mathbf{B}_m$ and Sun sensor measurement $\mathbf{B}_s$ are available.

The Procrustes problem is derived for both cases and the algorithm allows to switch between them. In each case, measurements are complemented by an additional modelled vector $\mathbf{B}_a$ associated to a virtual measurement. The solution to this problem is given as a rotation matrix using an SVD formulation [31].

In this section, the MAP optimisation objective is formulated for the satellite attitude determination problem. The solution to the optimisation problem is then derived in the first case of a Sun occlusion and in the second case where both measurements are available. The MAP calculation is then derived from the SVD solution and the conditional mean. The SVD-LPF algorithm is finally introduced.

4.1. The MAP computation

The MAP from equation (33) can be difficult to compute, especially when the state-space dimension is large. However, the MAP calculation simplifies when the likelihood only depends on part of the state vector $\mathbf{x}$.
Let $\mathbf{x} = \left[\mathbf{x}_1^T, \mathbf{x}_2^T\right]^T$ with $\mathbf{x}_1 = [q_0, q_1, q_2, q_3]^T$ and $\mathbf{x}_2 = [\omega_1, \omega_2, \omega_3]^T$. The posterior density $p(\mathbf{x}|\mathbf{y})$ can be written as:

$$\begin{aligned} p(\mathbf{x}|\mathbf{y}) &\propto p(\mathbf{y}|\mathbf{x})\, q(\mathbf{x}) \\ &= p(\mathbf{y}|\mathbf{x}_1, \mathbf{x}_2)\, q(\mathbf{x}_2|\mathbf{x}_1)\, q(\mathbf{x}_1). \end{aligned} \tag{37}$$

Therefore, the MAP calculation can be broken down as follows:

$$\max_{(\mathbf{x}_1, \mathbf{x}_2)} p(\mathbf{x}_1, \mathbf{x}_2|\mathbf{y}) = \max_{\mathbf{x}_1} \underbrace{p(\mathbf{y}|\mathbf{x}_1, \mathbf{x}_2)\, q(\mathbf{x}_1)}_{U(\mathbf{x}_1, \mathbf{x}_2)} \max_{\mathbf{x}_2} q(\mathbf{x}_2|\mathbf{x}_1). \tag{38}$$

The initial maximisation over the vector $\mathbf{x}$ is reframed into two separate maximisation problems, one over $\mathbf{x}_1$ and the other over $\mathbf{x}_2$.

- Maximisation of $U(\mathbf{x}_1, \mathbf{x}_2)$:
  In our case, $U(\mathbf{x}_1, \mathbf{x}_2) = U(\mathbf{x}_1)$ is maximised relative to $\mathbf{x}_1$. The prior

density $q(\mathbf{x}_1, \mathbf{x}_2)$ is assumed to be Gaussian of mean $[\mathbb{E}(\mathbf{x}_1), \mathbb{E}(\mathbf{x}_2)]^T = \left[\mathbf{q}^{-T}, \boldsymbol{\omega}^{-T}\right]^T$ and the covariance matrix:

$$\mathbf{P}^- = \begin{pmatrix} \mathbf{P}_{11}^- & \mathbf{P}_{12}^- \\ \mathbf{P}_{21}^- & \mathbf{P}_{22}^- \end{pmatrix}, \tag{39}$$

where:

- $\mathbf{q}^-$ is the prior quaternion,
- $\boldsymbol{\omega}^-$ is the prior angular velocity,
- $\mathbf{P}_{11}^-$ is the prior covariance sub-matrix of the quaternion part of $\mathbf{x}$,
- $\mathbf{P}_{22}^-$ is the prior covariance sub-matrix of the angular velocity part of $\mathbf{x}$,
- $\mathbf{P}_{12}^- = \mathbf{P}_{21}^{-T}$ is the prior cross-covariance sub-matrix between quaternion and the angular velocity vectors.

Assuming that the noises of the measurements of the magnetometer given by equation (18) and of the Sun sensor from equation (13) are Gaussian, the problem of finding $\mathbf{q}$ that optimises $U(\mathbf{x}_1)$, which is also part of the solution (38), can be written as:

$$\min_{\mathbf{q}}(\|\mathbf{Y}_s - \mathbf{R}(\mathbf{q})\mathbf{B}_s\|^2_{\Sigma_s} + \|\mathbf{Y}_m - \mathbf{R}(\mathbf{q})\mathbf{B}_m\|^2_{\Sigma_m} + \|\mathbf{q} - \mathbf{q}^-\|^2_{\mathbf{P}_{11}}), \tag{40}$$

where $\|\mathbf{q} - \mathbf{q}^-\|^2_{\mathbf{P}_{11}^-}$ represents the prior information. This term can be written as a new measurement model based on the attitude matrix $\mathbf{R}$ as following:

$$\|\mathbf{Y}_a - \mathbf{R}\mathbf{B}_a\|^2_{\Sigma_a}, \tag{41}$$

where $\mathbf{Y}_a$ represents the *a priori* information on the basis of the predicted rotation matrix $\mathbf{R}^-$ which depends on the past measurements. $\mathbf{Y}_a$ is modeled as follows:

$$\mathbf{Y}_a = \mathbf{R}^-\mathbf{B}_a = \mathbf{R}\mathbf{B}_a + \boldsymbol{\nu}_a. \tag{42}$$

$\mathbf{R}^- = \mathbf{R}(\mathbf{q}^-)$ is the predicted attitude matrix and $\boldsymbol{\nu}_a$ is the virtual *a priori* measurement noise. $\mathbf{B}_a$ and Σ_a will be described in propositions 2 and 3. Using the model of equation (42), the previous optimisation problem (40) can be rewritten as:

$$\mathbf{R}^* = \arg\min_{\mathbf{R}}(\|\mathbf{Y}_s - \mathbf{R}\mathbf{B}_s\|^2_{\Sigma_s} + \|\mathbf{Y}_m - \mathbf{R}\mathbf{B}_m\|^2_{\Sigma_m} + \|\mathbf{Y}_a - \mathbf{R}\mathbf{B}_a\|^2_{\Sigma_a}), \tag{43}$$

where $\mathbf{R}$ is a rotation matrix. In the remainder of this article, it is assumed that the Sun and magnetic field vectors have the same accuracy on all three axes: $\Sigma_s = \sigma_s^2\mathbf{I}_d$, $\Sigma_m = \sigma_m^2\mathbf{I}_d$ and $\Sigma_a = \sigma_a^2\mathbf{I}_d$ where σ_s^2 , σ_m^2 and σ_a^2 are the variances of the measurement noise of the Sun sensor, magnetometer and

$\mathbf{Y}_a$, respectively. Under this hypothesis, the solution $\mathbf{R}^*$ of equation (43) can be obtained explicitly using the Procrustes algorithm. This algorithm is described in the next subsection in its SVD decomposition formulation. In the case of a correlation between three axes, one should consider using a nonlinear method [32] for the computation of the MAP, although this would lead to a higher computational demand. The LPF presented in the paper (see Subsection 3.3) can therefore be applied to the case of axes correlations.

- Maximisation of $q(\mathbf{x}_2|\mathbf{x}_1)$:

  The conditional density $q(\mathbf{x}_2|\mathbf{x}_1)$ is Gaussian with $\mathbb{E}_{2|1}(\mathbf{x}_1) = \mathbb{E}(\mathbf{x}_2|\mathbf{x}_1)$ as a mean and $\mathbf{P}^-_{2|1}$ as a covariance matrix. The optimisation problem with respect to $\boldsymbol{\omega}$ given a value of $\mathbf{q}$ is written as:

$$\min_{\boldsymbol{\omega}} \|\boldsymbol{\omega} - \mathbb{E}_{2|1}(\mathbf{q})\|^2_{\mathbf{P}^-_{2|1}}, \tag{44}$$

  where

$$\mathbb{E}_{2|1}(\mathbf{q}) = \boldsymbol{\omega}^- + \mathbf{P}^-_{21}\left(\mathbf{P}^-_{11}\right)^{-1}\left(\mathbf{q} - \mathbf{q}^-\right).$$
$$\mathbf{P}^-_{2|1} = \mathbf{P}^-_{22} - \mathbf{P}^-_{21}\left(\mathbf{P}^-_{11}\right)^{-1}\mathbf{P}^-_{12}.$$

  As in the case of equation (43) which has an analytical solution $\mathbf{R}^*$, the solution of equation (44) can also be obtained analytically and is given by the conditional mean where the maximum of the Gaussian conditional density is reached:

$$\boldsymbol{\omega}^* = \mathbb{E}_{2|1}(\mathbf{q}^*), \tag{45}$$

  where $\mathbf{q}^*$ is the associated quaternion of $\mathbf{R}^*$

In conclusion, as we will see, an exact solution to the MAP of equation (38) noted $\mathbf{x}^* = \left[\mathbf{q}^{*T}, \boldsymbol{\omega}^{*T}\right]^T$ can be analytically calculated.

4.2. Attitude matrix calculation in the case of Sun occlusion

This section presents the solution to the attitude matrix calculation problem in the case of Sun occlusion. The rotation matrix is obtained by solving a constrained optimisation problem. The attitude of the satellite is estimated by the Procrustes method using the magnetic field vector measurements denoted by $\mathbf{B}_m$ and the predicted measurement $\mathbf{Y}_a$ given by equation (42). $\mathbf{B}_a$ will be described in the next propositions.

The following constrained optimisation problem, known as the Procrustes problem, provides the MAP relative to the quaternion $\mathbf{q}$ from equation (40), which leads to the estimation of the rotation matrix $\mathbf{R}^*$:

$$\min_{\substack{\mathbf{R}^T\mathbf{R}=\mathbf{I}_n \\ \det(\mathbf{R})=1}} (\mathbf{Y}_m - \mathbf{R}\mathbf{B}_m)^T\Sigma_m^{-1}(\mathbf{Y}_m - \mathbf{R}\mathbf{B}_m) + (\mathbf{Y}_a - \mathbf{R}\mathbf{B}_a)^T\Sigma_a^{-1}(\mathbf{Y}_a - \mathbf{R}\mathbf{B}_a), \tag{46}$$

where $\mathbf{B}_a$ and $\mathbf{B}_m$ are unit vectors.

$$\|\mathbf{B}_m\|^2 = \|\mathbf{B}_a\|^2 = 1. \tag{47}$$

Problem (46) boils down to a Procrustes problem and can be solved using Lagrange Multipliers. After some manipulations, the quadratic form equation (46) can be written as follows:

$$\begin{aligned} f(\mathbf{R}) = &-2\,\mathrm{Tr}\left\{\left(\frac{1}{\sigma_m^2}\mathbf{B}_m\mathbf{Y}_m^T + \frac{1}{\sigma_a^2}\mathbf{B}_a\mathbf{Y}_a^T\right)\mathbf{R}\right\} + \\ &\frac{1}{\sigma_m^2}\mathbf{B}_m^T\mathbf{R}^T\mathbf{R}\mathbf{B}_m + \frac{1}{\sigma_a^2}\mathbf{B}_a^T\mathbf{R}^T\mathbf{R}\mathbf{B}_a + \mathrm{Tr}(\mathbf{L}(\mathbf{R}^T\mathbf{R} - \mathbf{I}_n)) + \lambda(\det(\mathbf{R}) - 1), \end{aligned} \tag{48}$$

where $\mathbf{L}$ is a symmetric matrix of unknown Lagrange multipliers and λ is another unknown Lagrange multiplier. By setting to zero the partial derivatives of f with respect to $\mathbf{R}$, the following equation is obtained:

$$\begin{aligned} \frac{\partial f}{\partial \mathbf{R}} &= -2\mathbf{M}^T + \frac{2}{\sigma_m^2}\mathbf{R}\mathbf{B}_m\mathbf{B}_m^T + \frac{2}{\sigma_a^2}\mathbf{R}\mathbf{B}_a\mathbf{B}_a^T + 2\mathbf{L}\mathbf{R} + \lambda\det(\mathbf{R})\mathbf{R} \\ &= 0, \end{aligned} \tag{49}$$

where $\mathbf{M}$ is given by:

$$\mathbf{M} = \frac{1}{\sigma_m^2}\mathbf{B}_m\mathbf{Y}_m^T + \frac{1}{\sigma_a^2}\mathbf{B}_a\mathbf{Y}_a^T. \tag{50}$$

The equation (49) leads to:

$$\mathbf{R}\mathbf{N} = \mathbf{M}, \tag{51}$$

where $\mathbf{N}$ is given by:

$$\mathbf{N} = \frac{1}{\sigma_m^2}\mathbf{B}_m\mathbf{B}_m^T + \frac{1}{\sigma_a^2}\mathbf{B}_a\mathbf{B}_a^T + \mathbf{L} + \frac{\lambda}{2}\mathbf{I}_d, \tag{52}$$

The solution of the equation (51) is given by the following proposition.

Proposition 1. *The solution to the constrained optimisation problem of equation* (46) is given by:

$$\mathbf{R}^* = \mathbf{U}\mathbf{V}^\mathbf{T}, \tag{53}$$

where $\mathbf{M}$ from equation (50) has the following SVD decomposition,

$$\mathbf{M} = \mathbf{U}\Lambda\mathbf{V}^\mathbf{T}, \tag{54}$$

and where

$$\Lambda = \mathrm{diag}(1, 1, \det(\mathbf{U}\mathbf{V}^\mathbf{T})).$$

Proof. Since $\mathbf{N}$ in equation (51) is a symmetric matrix, it has the following SVD decomposition:

$$\mathbf{N} = \mathbf{V_1}\mathbf{\Lambda_1}\mathbf{V_1^T}, \tag{55}$$

where $\mathbf{V_1}$ is unitary matrix. By multiplying by $\mathbf{R}$ both sides of equation (55), we have:

$$\mathbf{RN} = (\mathbf{RV_1})\mathbf{\Lambda_1}\mathbf{V_1^T}. \tag{56}$$

Likewise, $\mathbf{M}$ also has an SVD decomposition:

$$\mathbf{M} = \mathbf{U}\Lambda\mathbf{V^T}. \tag{57}$$

Noting that $\mathbf{U}_1 = \mathbf{RV_1}$ is an orthogonal matrix, $\mathbf{RN} = \mathbf{U}_1\Lambda_1\mathbf{V_1^T}$ from equation (56) is the SVD decomposition of $\mathbf{RN}$ which is none other than that of $\mathbf{M}$ given by equation (51). Thanks to the unicity of the SVD decomposition, by identification in equation (57), we obtain: $\mathbf{U} = \mathbf{U}_1$, $\Lambda = \Lambda_1$ and $\mathbf{V} = \mathbf{V_1}$. Hence, the SVD decomposition of $\mathbf{N}$ is: $\mathbf{N} = \mathbf{V\Lambda V^T}$. The matrix $\mathbf{R}^*$ given by equation (53) satisfies equation (51). Indeed, we have:

$$\mathbf{R}^*\mathbf{N} = (\mathbf{UV^T})(\mathbf{V\Lambda V^T}) = \mathbf{U\Lambda V^T} = \mathbf{M}. \tag{58}$$

□

Now, we aim to optimise the parameters $\mathbf{B}_a$ and $\Sigma_a = \sigma_a^2\mathbf{I}_d$ defining the predicted measurement model of equation (42) in the case of Sun occlusion.

Proposition 2. *In the case of the Sun occlusion, the optimal predicted measurement model parameters that minimise the estimation error on the rotation matrix that solves the observation equations are obtained as follows:*

- *We choose the vector* $\mathbf{B}_a$ *to be orthogonal to* $\mathbf{B}_m$ *such that,*

$$\mathbf{B}_a = \begin{bmatrix} B_{m_2}/\sqrt{B_{m_1}^2 + B_{m_2}^2} \\ -B_{m_1}/\sqrt{B_{m_1}^2 + B_{m_2}^2} \\ 0 \end{bmatrix}, \tag{59}$$

  where $\mathbf{B}_m = [B_{m_1}, B_{m_2}, B_{m_3}]^T$.

  The vector $\mathbf{B}_a$ *then minimises the average error on the rotation matrix estimation* $\mathbf{R}^*$ *given by equation* (53).

- The covariance matrix of the predicted measurement $\mathbf{Y}_a$ adapted to the model of equation (43) is the following,

$$\Sigma_a = \sigma_a^2\mathbf{I}_d = \frac{1}{3}\,\mathrm{Tr}(\Sigma)\,\mathbf{I}_d, \tag{60}$$

  Σ being defined by:

$$\Sigma = \left.\frac{\partial\mathcal{L}}{\partial\mathbf{q}}\right|_{\mathbf{q}=\mathbf{q}^-} \mathbf{P}_{11}^- \left.\frac{\partial\mathcal{L}}{\partial\mathbf{q}}\right|_{\mathbf{q}=\mathbf{q}^-}, \tag{61}$$

  where $\mathcal{L}(\mathbf{q}) = \mathbf{R}(\mathbf{q})\mathbf{B}_a$, $\mathbf{P}_{11}^-$ from equation (39) being the covariance matrix of the predicted quaternions $\mathbf{q}^-$.

Proof. Perturbation theory [33] is used to determine the optimal choice of $\mathbf{B}_a$ in the sense of minimising the error on $\mathbf{R}^*$ given by equation (53). Consider the following matrix $\mathbf{W}$:

$$\mathbf{W} = \frac{1}{\sigma_m^2}\mathbf{B}_m\mathbf{B}_m^T + \frac{1}{\sigma_a^2}\mathbf{B}_a\mathbf{B}_a^T. \tag{62}$$

In [34], it is proven that, on average, the error on $\mathbf{R}^*$ is proportional to the so-called condition number:

$$\kappa = \left(\lambda_2^2 + \lambda_3^2\right)^{-\frac{1}{2}}, \tag{63}$$

where λ_i is the i^{th} ordered singular value of $\mathbf{W}$ such that $\lambda_1 \geq \lambda_2 \geq \lambda_3$.
For the sake of clarity, the variances σ_i^2 are omitted in the proof:

$$\mathbf{W} = \mathbf{B}_m\mathbf{B}_m^T + \mathbf{B}_a\mathbf{B}_a^T, \tag{64}$$

The matrix $\mathbf{W}$ is positive definite and is of rank 2 if $\mathbf{B}_a$ and $\mathbf{B}_m$ are linearly independent and its singular values are coincident with the eigenvalues. Observing that $\mathrm{Tr}(\mathbf{W}) = 2$, the eigenvalues of $\mathbf{W}$ are: $(\lambda_1, \lambda_2, \lambda_3)^T = (\alpha, 2-\alpha, 0)^T$ with $1 \leq \alpha \leq 2$. It suffices to establish that, for some value of $\mathbf{B}_a$, $\lambda_2 = 1$ is an eigenvalue of $\mathbf{W}$ to ensure that the minimal value of the condition number κ from equation (63) that maximises $(2-\alpha)$. This is the case if $\mathbf{B}_a$ is orthogonal to $\mathbf{B}_m$. Indeed, we have:

$$\begin{aligned}
\mathbf{WW} &= (\mathbf{B}_m\mathbf{B}_m^T + \mathbf{B}_a\mathbf{B}_a^T)(\mathbf{B}_m\mathbf{B}_m^T + \mathbf{B}_a\mathbf{B}_a^T) \\
&= \mathbf{B}_m\mathbf{B}_m^T\mathbf{B}_m\mathbf{B}_m^T + \mathbf{B}_m\mathbf{B}_m^T\mathbf{B}_a\mathbf{B}_a^T + \mathbf{B}_a\mathbf{B}_a^T\mathbf{B}_m\mathbf{B}_m^T + \mathbf{B}_a\mathbf{B}_a^T\mathbf{B}_a\mathbf{B}_a^T \\
&= \mathbf{B}_m\mathbf{B}_m^T + \mathbf{B}_a\mathbf{B}_a^T \\
&= \mathbf{W},
\end{aligned}$$

since $\mathbf{B}_m^T\mathbf{B}_m = \mathbf{B}_a^T\mathbf{B}_a = 1$ and $\mathbf{B}_m^T\mathbf{B}_a = 0$. A possible choice of $\mathbf{B}_a$ is the one from equation (59). Another way to determine $\mathbf{B}_a$, which minimises the condition number from equation (63), consists in solving the following optimisation problem:

$$\min_{\|\mathbf{B}_a\|=1} \|\mathbf{B}_m\mathbf{B}_m^T + \mathbf{B}_a\mathbf{B}_a^T - \tilde{\mathbf{I}}_d\|^2, \tag{65}$$

where

$$\tilde{\mathbf{I}}_d = \begin{pmatrix} 1 & 0 & 0 \\ 0 & 1 & 0 \\ 0 & 0 & 0 \end{pmatrix}, \tag{66}$$

which gives the same result. Having defined $\mathbf{B}_a$, it remains necessary to compute the covariance matrix Σ_a of the predicted measurement model of equation (42). Let $\mathcal{L}(\mathbf{q}) = \mathbf{R}(\mathbf{q})\mathbf{B}_a$, the 1^{st} order Taylor expansion of the function $\mathcal{L}(\mathbf{q})$ around $\mathbf{q}_0$ is given by:

$$\mathbf{Y}_a \approx \mathcal{L}(\mathbf{q}_0) + \left.\frac{\partial \mathcal{L}}{\partial \mathbf{q}}\right|_{\mathbf{q}=\mathbf{q}_0} (\mathbf{q} - \mathbf{q}_0), \tag{67}$$

which leads to the following covariance matrix approximation (see Appendix):

$$\Sigma \approx \left.\frac{\partial \mathcal{L}}{\partial \mathbf{q}}\right|_{\mathbf{q}=\mathbf{q}^-} \mathbf{P}_{11}^- \left.\frac{\partial \mathcal{L}}{\partial \mathbf{q}}\right|_{\mathbf{q}=\mathbf{q}^-}, \tag{68}$$

where $\mathbf{P}_{11}^- = \mathbf{P}_{\mathbf{q}^-}$ is the covariance matrix of the predicted quaternions $\mathbf{q}^-$. Σ is an approximation of the covariance matrix of $\mathbf{Y}_a$. However, the latter is not adapted to the Procrustes problem, which requires the covariance matrix to be diagonal (see Proposition 1). A diagonal matrix Σ_a, which best approximates Σ will therefore need to be estimated:

$$\min_{\lambda} \|\Sigma - \lambda \mathbf{I}_d\|^2. \tag{69}$$

It is easily verified that $\lambda = \frac{1}{3}\operatorname{Tr}(\Sigma)$ yields this minimum. Therefore, the covariance matrix Σ_a of the predicted measurement modelled using equation (42) is the following:

$$\Sigma_a = \sigma_a^2 \mathbf{I}_d = \frac{1}{3}\operatorname{Tr}(\Sigma)\mathbf{I}_d. \tag{70}$$

□

4.3. Attitude matrix calculation with magnetic field measurement and Sun sensing

In this case, the attitude of the satellite is also estimated using the Procrustes method. The constrained optimisation problem now takes the following form:

$$\min_{\substack{\mathbf{R}^T\mathbf{R}=\mathbf{I}_d \\ \det(\mathbf{R})=1}} (\mathbf{Y}_s - \mathbf{R}\mathbf{B}_s)^T \Sigma_s^{-1} (\mathbf{Y}_s - \mathbf{R}\mathbf{B}_s) + (\mathbf{Y}_m - \mathbf{R}\mathbf{B}_m)^T \Sigma_m^{-1} (\mathbf{Y}_m - \mathbf{R}\mathbf{B}_m) + (\mathbf{Y}_a - \mathbf{R}\mathbf{B}_a)^T \Sigma_a^{-1} (\mathbf{Y}_a - \mathbf{R}\mathbf{B}_a). \tag{71}$$

We obtain the solution of this constrained optimisation problem:

$$\mathbf{R}^* = \mathbf{U}\mathbf{V}^\mathbf{T}, \tag{72}$$

where

$$\mathbf{M} = \frac{1}{\sigma_s^2}\mathbf{B}_s\mathbf{Y}_s^T + \frac{1}{\sigma_m^2}\mathbf{B}_m\mathbf{Y}_m^T + \frac{1}{\sigma_a^2}\mathbf{B}_a\mathbf{Y}_a^T, \tag{73}$$

has the following SVD decomposition:

$$\mathbf{M} = \mathbf{U}\Lambda\mathbf{V}^\mathbf{T}. \tag{74}$$

As previously described, the aim is to optimise the parameters $\mathbf{B}_a$ and $\Sigma_a = \sigma_a^2\mathbf{I}_d$, which define the predicted measurement model of equation (42) in the case of magnetic field and Sun sensor measurements.

Proposition 3. *When the Sun sensor and magnetic field measurements are both available, the optimal parameters of the predicted measurement model that minimise the estimation error on the rotation matrix that solves the observation equations are obtained as follows:*

- *The vector* $\mathbf{B}_a$ *is chosen to be orthogonal to the plane formed by the two vectors* $\mathbf{B}_s$ *and* $\mathbf{B}_m$ *and is given by:*

$$\mathbf{B}_a = \frac{\mathbf{B}_s \times \mathbf{B}_m}{\|\mathbf{B}_s \times \mathbf{B}_m\|}, \tag{75}$$

  This choice of $\mathbf{B}_a$ *minimises the average error on the rotation matrix estimation* $\mathbf{R}^*$ *given by equation* (72).

- The covariance matrix of the predicted virtual measurement vector $\mathbf{Y}_a$ adapted to the model of equation (43) is given by:

$$\Sigma_a = \sigma_a^2 \mathbf{I}_d = \frac{1}{3}\operatorname{Tr}(\Sigma)\,\mathbf{I}_d, \tag{76}$$

  where Σ is defined as:

$$\Sigma = \left.\frac{\partial \mathcal{L}}{\partial \mathbf{q}}\right|_{\mathbf{q}=\mathbf{q}^-} \mathbf{P}_{11}^- \left.\frac{\partial \mathcal{L}}{\partial \mathbf{q}}\right|_{\mathbf{q}=\mathbf{q}^-}, \tag{77}$$

  where $\mathcal{L}(\mathbf{q}) = \mathbf{R}(\mathbf{q})\mathbf{B}_a$, $\mathbf{P}_{11}^-$ is given by equation (39) is the covariance matrix of the predicted quaternion $\mathbf{q}^-$.

Proof. The proof is similar to that of Proposition 2. The aim is to estimate $\mathbf{B}_a$ in order to minimise the condition number κ from equation (63). This is achieved by minimising the following criterion (65):

$$\min_{\|\mathbf{B}_a\|=1} f(\mathbf{B}_a) = \min_{\|\mathbf{B}_a\|=1} \|\mathbf{W} - \mathbf{I}_d\|^2, \tag{78}$$

where $\mathbf{W} = \mathbf{B}_s\mathbf{B}_s^T + \mathbf{B}_m\mathbf{B}_m^T + \mathbf{B}_a\mathbf{B}_a^T$ is a matrix of rank 3. After some manipulations, it can be shown that $f(\mathbf{B}_a)$ simplifies to the following expression:

$$f(\mathbf{B}_a) = 2\operatorname{Tr}(\mathbf{B}_s\mathbf{B}_s^T\mathbf{B}_m\mathbf{B}_m^T + \mathbf{B}_s\mathbf{B}_s^T\mathbf{B}_a\mathbf{B}_a^T + \mathbf{B}_m\mathbf{B}_m^T\mathbf{B}_a\mathbf{B}_a^T). \tag{79}$$

Clearly, $f(\mathbf{B}_a)$ is minimised when $\mathbf{B}_a$ is orthogonal to both $\mathbf{B}_s$ and $\mathbf{B}_m$. Under this condition, we have: $f(\mathbf{B}_a) = 2\operatorname{Tr}(\mathbf{B}_s\mathbf{B}_s^T\mathbf{B}_m\mathbf{B}_m^T) \geq 0$. □

4.4. Discussion on the approximation of the covariance matrix of the predicted virtual measurement

In using an approximate diagonal covariance matrix for the predicted virtual measurement from equations (70) and (76), the MAP estimate $\mathbf{x}_k^*$, which occurs in the SVD-LPF resampling step (see Algorithm 2) is slightly biased. The particle filter samples around this approximate MAP given by equation (36).

The bias of the MAP affects the variance of the Monte Carlo approximation of the posterior estimate $\mathbb{V}[\hat{\mathbf{x}}_k]$, where $\hat{\mathbf{x}}_k$ is obtained from Algorithm 2. However, the mean value of the posterior estimate $\mathbb{E}[\hat{\mathbf{x}}_k]$ remains unbiased [35, 17]. The numerical simulations (see Subsection 5.2) show that the MAP bias has no significant impact on the attitude estimation accuracy.

4.5. Maximum A Posteriori calculation

The MAP calculation takes as inputs the prior knowledge of the attitude quaternion, the angular velocity and the prior covariance matrix to solve the Procrustes problem. The Procrustes attitude solution is then used to compute the MAP as a concatenation of two subvectors:

- The MAP attitude quaternion is taken as the Procrustes problem solution;
- The MAP angular velocity is computed from the quaternion using the conditional expectancy principle.

The MAP covariance is assumed to be equal to the prior covariance. The MAP calculation is described in Algorithm 1.

Algorithm 1 MAP calculation

Measurement $\mathbf{Y}_a$ and covariance matrix Σ_a calculation:

- Get the predicted quaternion $\mathbf{q}^-$ and the predicted angular velocity $\boldsymbol{\omega}^-$;
- Get the predicted covariance matrix $\mathbf{P}^-$ from Equation (39);
- Compute the predicted attitude matrix $\mathbf{R}^- = \mathbf{R}(\mathbf{q}^-)$;
- Compute the a priori vector $\mathbf{B}_a$ from Equation (59) or (75);
- Compute the vector $\mathbf{Y}_a$ from Equation (42);
- Compute the covariance matrix Σ_a from Proposition 2 during Sun occlusion or Proposition 3 during the sunlit phase.

Calculating the attitude matrix:

- Compute the Procrustes attitude Matrix solution $\mathbf{R}^*$ from Equation (53) or (72) by adapting the formulation to the number of available sensors (see Sections 4.2 and 4.3);
- Convert matrix $\mathbf{R}^*$ to the associated quaternion $\mathbf{q}^*$ using Shepperd's method [36].

Calculating the MAP $\mathbf{x}^*$:

- Compute the angular velocity vector $\boldsymbol{\omega}^*$ from Equation (45);
- Get the MAP $\mathbf{x}^* = \left[\mathbf{q}^{*T}, \boldsymbol{\omega}^{*T}\right]^T$.

4.6. SVD-LPF algorithm

The SVD-LPF algorithm is based on the LPF principle and uses the MAP calculation algorithm presented in Algorithm 1. The pseudo-code of the SVD-LPF is presented in Algorithm 2.

Algorithm 2 The SVD-Laplace Particle Filter

Initialisation:
The initial particle set is drawn as $\left\{\mathbf{x}_0^i = \left[\mathbf{q}_0^{i\,T}, \boldsymbol{\omega}_0^{i\,T}\right]^T\right\}_{i\in[1,N]}$ using the initial density $p(\mathbf{x}_0)$, associated to weights $\omega_0^i = 1/N$.
for $k = 1, 2, ...$ **do**

- Prediction:
  The particles are drawn from prior density $\mathbf{x}_k^i \sim p(\mathbf{x}_k|\mathbf{x}_{k-1}^i)$ according to the dynamical equations (3) and (6).
  - Predicted mean:
    $\hat{\mathbf{x}}_{k|k-1} = \sum_{i=1}^N \omega_{k-1}^i \mathbf{x}_k^i \triangleq \left[\mathbf{q}^{-T}, \boldsymbol{\omega}^{-T}\right]^T$,
  - Predicted covariance matrix:
    $\mathbf{P}_{k|k-1} = \sum_{i=1}^N \omega_{k-1}^i (\mathbf{x}_k^i - \hat{\mathbf{x}}_{k|k-1})(\mathbf{x}_k^i - \hat{\mathbf{x}}_{k|k-1})^T \triangleq \mathbf{P}^-$.

- Correction:
  The weights are updated using the likelihood $\varpi_k^i = \omega_{k-1}^i\, g(\mathbf{x}_k^i)$.
  - Normalize the weights: $\omega_k^i = \frac{\varpi_k^i}{\sum_j^N \varpi_k^j}$.

- Laplacian resampling:
  if $N_{eff} < N_{th}$ **then**
  - Get the MAP: $\mathbf{x}_k^* = \left[\mathbf{q}_k^{*\,T}, \boldsymbol{\omega}_k^{*\,T}\right]^T$ from Algorithm 1,
  - Drawn particles from proposal density: $\mathbf{x}_k^i \sim \mathcal{N}(\mathbf{x}_k; \mathbf{x}_k^*, \mathbf{P}_{k|k-1})$,
  - Normalize the quaternions: $\mathbf{q}_k^i = \frac{\mathbf{q}_k^i}{\sum_{j=1}^N \mathbf{q}_k^j}$,
  - Weights update:

$$\begin{aligned}\varpi_k^i &= \frac{g(\mathbf{x}_k^i)\, q(\mathbf{x}_k^i)}{\tilde{q}(\mathbf{x}_k^i)}, \\ &= \frac{\mathcal{N}(\mathbf{y}_k; H_k(\mathbf{x}_k^i), \mathbf{R}_k)\, \mathcal{N}(\mathbf{x}_k^i; \hat{\mathbf{x}}_{k|k-1}, \mathbf{P}_{k|k-1})}{\mathcal{N}(\mathbf{x}_k^i; \mathbf{x}_k^*, \mathbf{P}_{k|k-1})},\end{aligned}$$

  where $g(.)$, $q(.)$ and $H_k(.)$ are defined in Equations (27) and (24) respectively.
  - Normalize the weights: $\omega_k^i = \frac{\varpi_k^i}{\sum_j^N \varpi_k^j}$.

  end if

Mean: $\hat{\mathbf{x}}_k = \sum_{i=1}^N \omega_k^i \mathbf{x}_k^i$,
Covariance matrix: $\mathbf{P}_k = \sum_{i=1}^N \omega_k^i (\mathbf{x}_k^i - \hat{\mathbf{x}}_k)(\mathbf{x}_k^i - \hat{\mathbf{x}}_k)^T$.
end for

5. Numerical simulation analysis and filters comparison

5.1. Operating conditions for the numerical simulation

A microsatellite model is considered here, with moments of inertia $I_{xx} = 19\ kg.m^2$, $I_{yy} = 19.5\ kg.m^2$, $I_{zz} = 12\ kg.m^2$, about the body X, Y and Z axes respectively. This corresponds to a nearly axisymmetric microsatellite. All filters under comparison are applied to the same model of natural satellite attitude dynamics. For simplicity, it is assumed that the reaction wheels operate in a zero momentum mode. The state vector is $\mathbf{x} = [q_0, q_1, q_2, q_3, \omega_x, \omega_y, \omega_z]^T$, where $\omega_x, \omega_y, \omega_z$ are the components of the inertially referenced angular velocity vector in body coordinates $\boldsymbol{\omega}$.

The mean initial conditions for the simulations are:
$\omega_x(0) = 0°/s$, $\omega_y(0) = -0.06°/s$, $\omega_z(0) = 0°/s$, $q_0(0) = 0.7861$, $q_1(0) = 0.1675$, $q_2(0) = 0.5709$ and $q_3(0) = 0.1675$, which corresponds to an attitude of 57.2838 degrees in roll, 57.2942 degrees in pitch and 57.2838 degrees in yaw angle, with respect to the local orbit frame.

Attitude estimation is obtained by data fusion from three orthogonal Sun sensors out of six when they are lit by the Sun and three orthogonal magnetometers, which is a commonly used combination for small medium resolution Earth observation satellites in a normal operation mode. It is assumed that the satellite is orbiting the Earth on a nearly circular low Earth orbit at an altitude of $650\,km$ with an inclination of 96 degrees. All simulations are performed for $6000\,s$ representing the duration of one satellite orbit.

The magnetometer and Sun sensor measurements are obtained with a sampling time for the measurement updates period of $1\,s$.

The measurement models are described in Section 2 and filter parameters including initial uncertainty and sensor standard deviations are given in the next subsection.

5.2. Numerical simulation results and analysis

In this section, the SVD-LPF and RPF are compared in terms of Root-Mean-Square Error (RMSE) for $N_{\text{MC}} = 100$ Monte Carlo runs. The RMSE is defined for any state variable x as:

$$RMSE(x_k) = \sqrt{\frac{\sum_{j=1}^{N_{\text{MC}}} \left(\hat{x}_k^j - x_k\right)^2}{N_{\text{MC}}}}, \tag{80}$$

where x_k and $\hat{x}_k^j$ respectively represent the true and estimated state variable at time step k for the j^{th} Monte Carlo run.

The average RMSE (ARMSE) over the total simulation time will also be used as an estimation performance metric and is given by:

$$ARMSE(x) = \frac{\sum_{k=1}^{N_s} RMSE(x_k)}{N_s}, \tag{81}$$

where N_s is the total number of time steps for the simulation. In our case, N_s is taken equal to 6000.

The numerical simulation comparison of the SVD-LPF and RPF filters is performed under two scenarios that differ in their magnetometer accuracies. The effect of magnetometer accuracy is particularly important because magnetometers are the only available sensors during solar eclipse.

The filters are compared in terms of state estimation accuracy and robustness to measurement discontinuity during eclipse for the same Sun sensor accuracy.

The simulation parameters are set as follows:

- The sampling time is $\triangle T = 1\,s$;
- The Sun sensor and magnetometer update frequencies are taken to be equal to 1 Hz;
- The initial uncertainty is characterised by the error covariance matrix, which is given by:

$$\mathbf{P}_0 = \text{diag}([(0.9972)^2,\ (0.0416)^2,\ (0.0454)^2,\ (0.0416)^2, \\ (0.1^\circ/s)^2,\ (0.1^\circ/s)^2,\ (0.1^\circ/s)^2]);$$

- The process noise covariance matrix is taken to be similar to the one in [37] and is given by:

$$\mathbf{Q}_k = 10^{-4}\,\text{diag}\left(\left[\frac{\triangle T^3}{12\ I_{xx}^2} + \frac{\triangle T^3}{12\ I_{yy}^2} + \frac{\triangle T^3}{12\ I_{zz}^2},\ \frac{\triangle T^3}{12\ I_{xx}^2}, \right.\right. \\ \left.\left. \frac{\triangle T^3}{12\ I_{yy}^2},\ \frac{\triangle T^3}{12\ I_{zz}^2}, \frac{\triangle T}{I_{xx}^2},\ \frac{\triangle T}{I_{yy}^2},\ \frac{\triangle T}{I_{zz}^2}\right]\right);$$

- The measurement noise covariance matrix is:

$$\mathbf{R}_k = \begin{cases} \text{diag}([\mathbf{R}_{Sun}, \mathbf{R}_{mag}]) & \text{during the sunlit phase,} \\ \mathbf{R}_{mag} & \text{during the Sun occlusion.} \end{cases}$$

- The threshold for the resampling criterion defined in equation (30) is $N_{th} = 0.75N$.

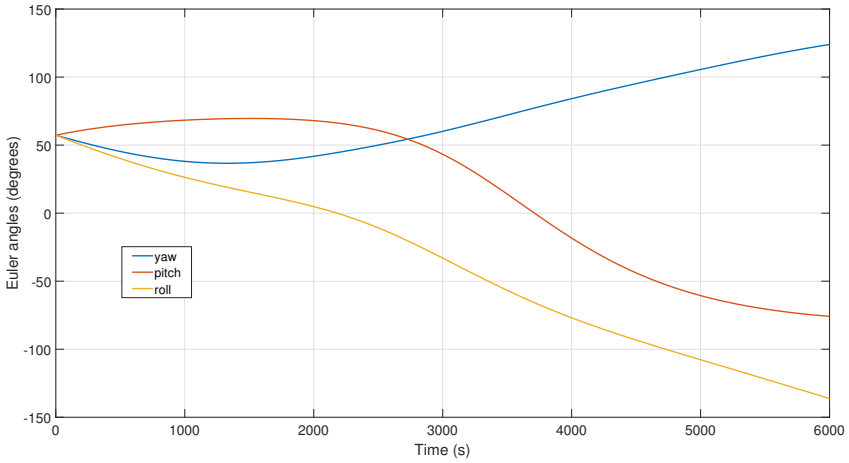

Figure 1: *The reference attitude (Euler angles) over 1 orbit (6000 s).*

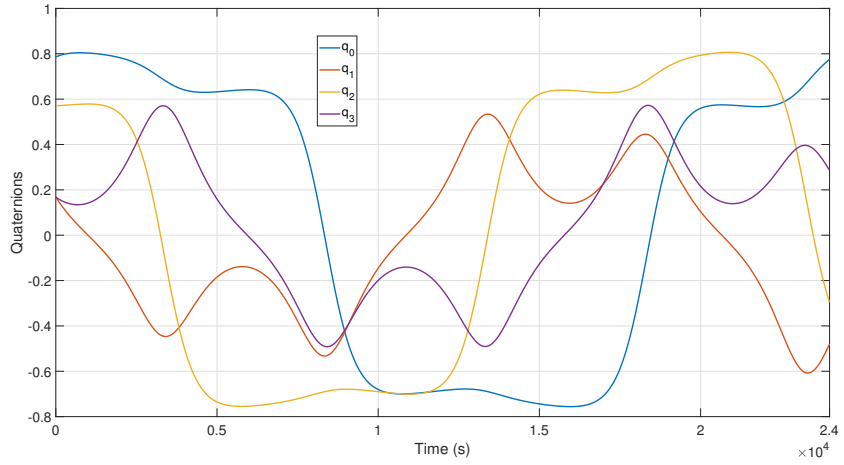

Figure 2: *The reference attitude (quaternions) over 4 orbits (24000 s).*

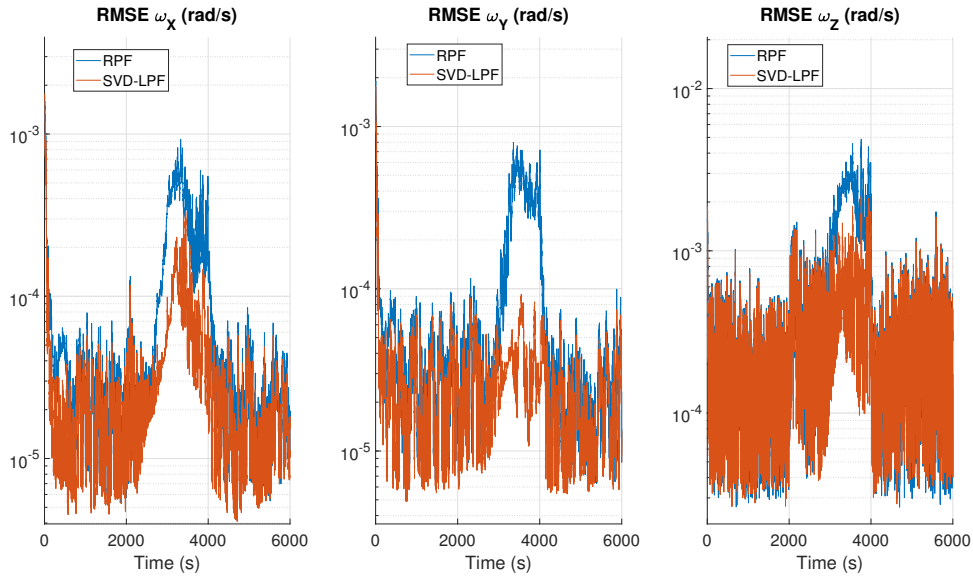

Figure 3: *RMSE of angular velocity estimation for the SVD-LPF and RPF under moderate magnetometer noise* $\mathbf{R}_{m_1}$ *(log scale on the y-axis).*

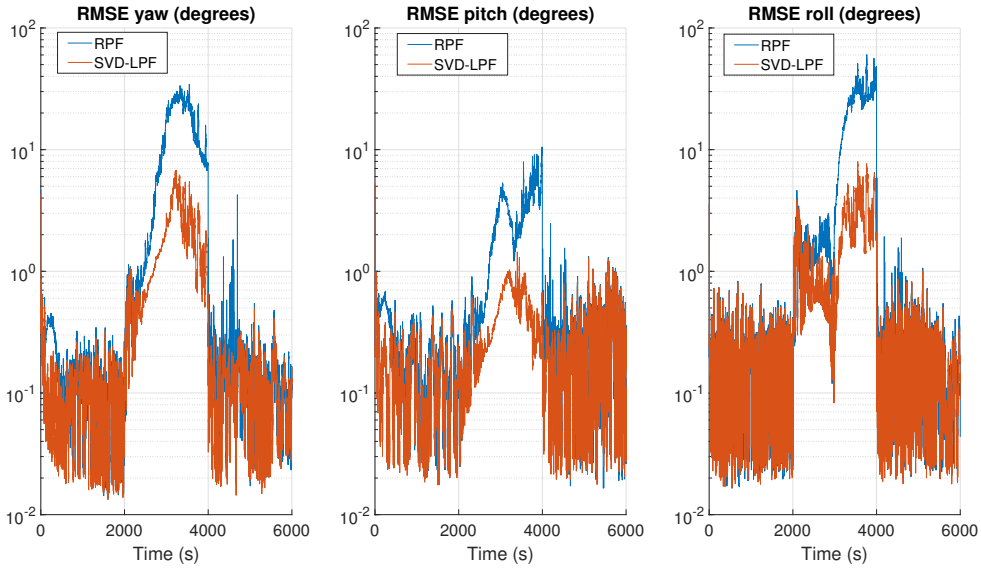

Figure 4: *RMSE of attitude estimation for the SVD-LPF and RPF under moderate magnetometer noise* $\mathbf{R}_{m_1}$ *(log scale on the y-axis).*

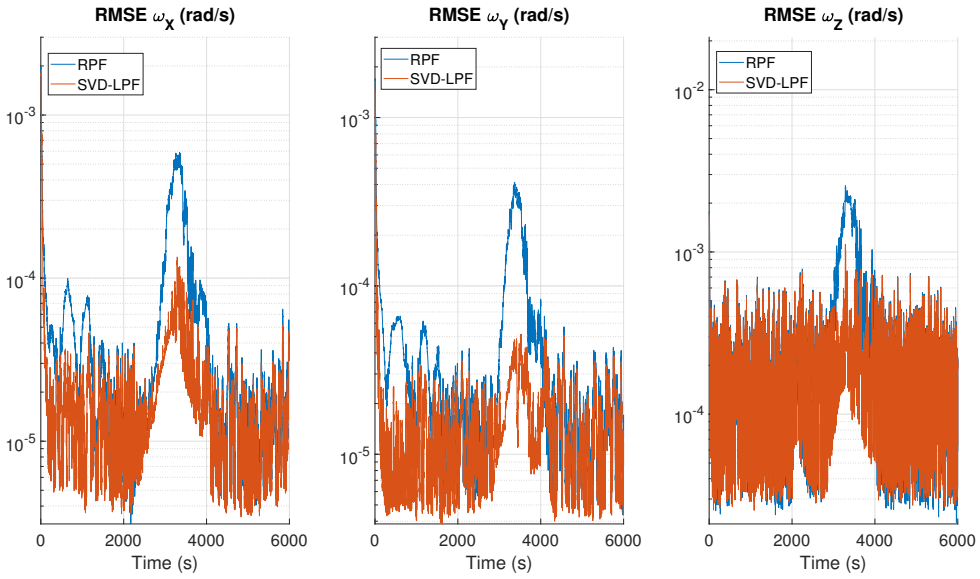

Figure 5: *RMSE of angular velocity estimation for the SVD-LPF and RPF under low magnetometer noise* $\mathbf{R}_{m_2}$ *(log scale on the y-axis).*

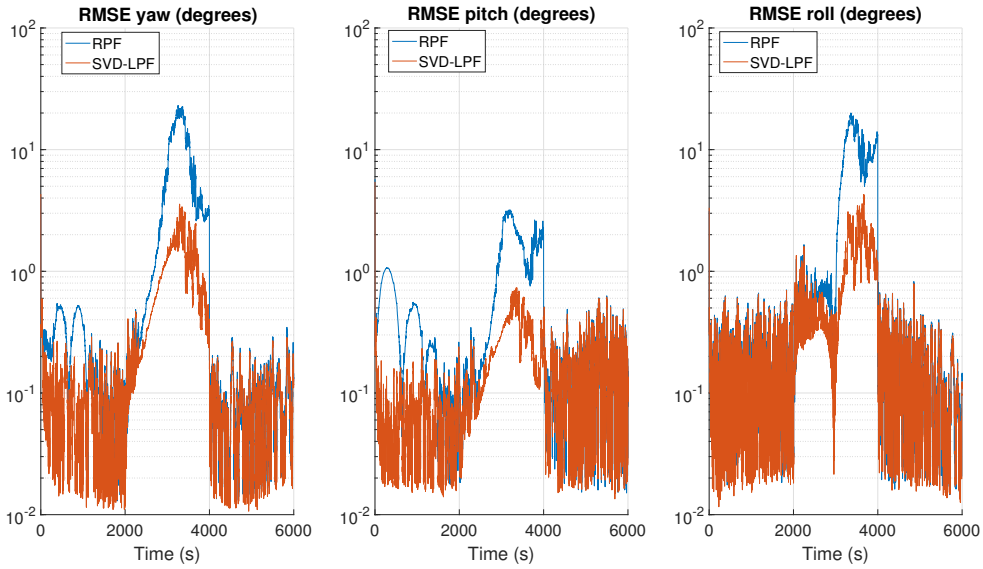

Figure 6: *RMSE of attitude estimation for the SVD-LPF and RPF under low magnetometer noise* $\mathbf{R}_{m_2}$ *(log scale on the y-axis).*

A similarity between the two scenarios under consideration is that simulation time is 1 orbit ($6000\,s$) and that the satellite eclipse occurs between $t = 2000\,s$ and $t = 4000\,s$ representing one third of the orbit. Both scenarios also have the same initial uncertainty of approximately 5 degrees on all three axes and the same Sun sensor accuracy when the satellite is not in a solar eclipse is given by: $\mathbf{R}_{Sun} = \text{diag}([(0.4^\circ)^2,\ (0.4^\circ)^2,\ (0.4^\circ)^2])$.

The difference between the scenarios is that magnetometer sensor noise levels are taken to be different. Two scenarios are considered, which are as follows:

- Scenario 1, magnetometer measurement noise covariance matrix is $\mathbf{R}_{mag} = \mathbf{R}_{m_1} = \text{diag}([(0.2\ \mu T)^2,\ (0.2\ \mu T)^2, (0.2\ \mu T)^2])$;
- Scenario 2, magnetometer measurement noise covariance matrix is $\mathbf{R}_{mag} = \mathbf{R}_{m_2} = \text{diag}([(0.02\ \mu T)^2,\ (0.02\ \mu T)^2, (0.02\ \mu T)^2])$.

The numbers of particles for the SVD-LPF and the RPF were chosen to be $N = 2000$.

The actual/reference attitude with respect to the local orbit frame is provided in Figure 1 (Euler angles) for 1 orbit (the time duration for the particle filtering simulations). In Figure 2, quaternions (body frame with regard to orbit frame) are displayed for 4 orbits to show the periodicity of the torque free motion. The period is 1 orbit because positive and negative quaternions correspond to the same physical orientation. The initial angular rate about the y-axis in the body frame is taken to match the orbital rate, but the y-axis of the local orbit frame is different from the initial body frame y-axis due to initial attitude error. The nonzero initial attitude with respect to the orbit frame means that the attitudes change on all three axes using a 3-2-1 Euler rotational sequence. The time derivatives of the roll, pitch and yaw are Euler sequence dependent and initial condition dependent and are different from the angular velocities about the instantaneous body axes. The attitude variations repeat every 1 orbit as expected and as shown in the quaternion figure.

The angular velocities and attitudes of scenarios 1 and 2 are respectively represented in Figures 3 to 6 and mostly differ in their maximum deviations during eclipse when the satellite is in the Earth's shadow. The attitude was converted from quaternions to Euler angles to simplify the results interpretation.

Figure 3 and Figure 4 with magnetometer covariance matrix $\mathbf{R}_{m_1}$ show that both filters are accurate before and after eclipse but that the SVD-LPF has a significantly lower RMSE. During solar eclipse, the SVD-LPF clearly outperforms the RPF with deviations not exceeding 8 degrees on all three axes, while the RPF deviation reaches up to 60 degrees about the roll axis, under the same initial uncertainty. The variance of the SVD-LPF is also significantly lower during both the sunlit and Sun occlusion phases.

Figure 5 and Figure 6 with the lower magnetometer covariance matrix $\mathbf{R}_{m_2}$ show further improvement with SVD-LPF accuracies below 5 degrees on all axes and below 1 degree on the pitch axis. The RPF accuracy also improves with a maximum deviation of 3 degrees on the pitch axis and about 20 degrees on

the other axes during eclipse. The SVD-LPF has significantly lower RMSE and variance during both the sunlit and Sun occlusion stages.

As shown in Figures 3 to 6, the estimation errors on the attitude and angular velocity are significantly lower with an improvement of up to one order of magnitude using the SVD-LPF in both cases of low and high sensor noise.

The ARMSE results are summarised in Table 1 and Table 2. In the case of one orbit (see in Table 1), the yaw ARMSE is reduced by a factor of 5.75 in scenario 1 (moderate magnetometer noise) and 5.51 in scenario 2 (low magnetometer noise). The pitch ARMSE is also reduced by a factor of 3.48 in scenario 1 and 3.52 in senario 2. Finally, the roll ARMSE is reduced by a factor of 5.82 in scenario 1 and 4.44 in scenario 2. During the solar eclipse (see Table 2), the yaw ARMSE is reduced by a factor of 6.27 in scenario 1 (moderate magnetometer noise) and 6.18 in scenario 2 (low magnetometer noise). The pitch ARMSE is reduced by a factor of 5.61 in scenario 1 and 4.61 in senario 2. Finally, the roll ARMSE is reduced by a factor of 6.80 in scenario 1 and 5.59 in scenario 2. The RMSE improvement is therefore significant in both cases of low and high magnetometer accuracies but is more pronounced overall when the magnetometer accuracy is lower and particularly during the solar eclipse.

Table 1: ARMSE results over 1 orbit ($6000\,s$)

	SVD-LPF	RPF
Scenario 1		
$ARMSE\ yaw$ (degrees)	0.6752	3.8888
$ARMSE\ pitch$ (degrees)	0.2777	0.9659
$ARMSE\ roll$ (degrees)	0.7608	4.4370
Scenario 2		
$ARMSE\ yaw$ (degrees)	0.3643	2.0098
$ARMSE\ pitch$ (degrees)	0.1593	0.5622
$ARMSE\ roll$ (degrees)	0.4315	1.9166

Table 2: ARMSE results during the solar eclipse

	SVD-LPF	RPF
Scenario 1		
$ARMSE\ yaw$ (degrees)	1.8088	11.3553
$ARMSE\ pitch$ (degrees)	0.4226	2.3726
$ARMSE\ roll$ (degrees)	1.8934	12.8821
Scenario 2		
$ARMSE\ yaw$ (degrees)	0.9231	5.7127
$ARMSE\ pitch$ (degrees)	0.2511	1.1595
$ARMSE\ roll$ (degrees)	0.9623	5.3861

5.3. Computational demand and real time implementation considerations

5.3.1. Complexity analysis

The complexity of algorithms can be evaluated in terms of their computational load for a given set of numerical operations. This complexity criterion is often used in state estimation [38]. The computational load is defined as the total number of floating point operations (or flops, namely additions and multiplications) required to perform them during one time-step (i.e., prediction, correction and Laplacien resampling for the SVD-LPF).

In this section, we compare the SVD-LPF approach with the classical Extended Kalman Filter (EKF) in terms of algorithmic complexity. In order to compare the SVD-LPF and the EKF, we assume that the dynamics are linearized. Table 3 presents the total number of flops and is obtained by adding the number of multiplications and additions. Moreover, some operations such as random numbers generation or highly nonlinear functions cannot be quantified in terms of flops. The cost of evaluating the Gaussian likelihood and the Laplacian resampling are denoted c_1 and c_2 respectively. The theoretical cost of one random sample is denoted c_3. Furthermore, for comparisons between filtering algorithms, only the most significant terms will be considered and are denoted by $\mathcal{O}(.)$.

Table 3: The flops complexity associated with elementary operations.

Instruction	Size	Multiplications	Additions
$A+B$	$A, B \in \mathbb{R}^{n\times m}$		nm
AB	$A \in \mathbb{R}^{n\times m}, B \in \mathbb{R}^{m\times l}$	nml	$(m-1)nl$
A^{-1}	$A \in \mathbb{R}^{n\times n}$	n^3	

The implementation of the EKF yields the following number of flops per time-step, as stated by [39]:

$$\mathcal{C}_{\text{EKF}} = \frac{3}{2}n^3 + n^2\left(3m + \frac{1}{2}n\right) + n\left(\frac{3}{2}m^2 + n^2\right) + \frac{1}{6}m^3, \tag{82}$$

where n and m are the dimension of the state vector and the observation vector respectively.

The SVD-LPF yields the following number of flops per time-step, assuming a linear dynamics, is given by:

$$\mathcal{C}_{\text{SVD-LPF}} = N\left(4n^2 + n + nc_3 + c_1 + c_2\right) + \frac{4}{3}n^3 + 2n^2, \tag{83}$$

where N is the number of particles.

Table 4: Computational load (flops) needed by SVD-LPF and EKF for $m < n$, $c_1 < n^2$, $c_2 < n^2$ and $c_3 < n^2$.

Algorithm	EKF	SVD-LPF
Prediction	$\mathcal{O}(n^3)$	$\mathcal{O}(Nn^2)$
Correction	$\mathcal{O}(n^2m)$	$\mathcal{O}(Nc_1)$
Laplacian resampling	-	$\mathcal{O}(Nc_2)$
Estimate	$\mathcal{O}(n^3)$	$\mathcal{O}(Nn^2)$
Total	$\mathcal{O}(n^3)$	$\mathcal{O}(Nn^2)$

From of the Equation (83), the number of particles N is the important factor in terms of computational load. Assuming that $m < n$ and that the costs of c_1, c_2 and c_3 are less than n^2, the first order term of the algorithm complexity of SVD-LPF per time step is $\mathcal{O}(Nn^2)$ and $\mathcal{O}(n^3)$ with EKF (see Table 4). Therefore, the global ratio between the two complexities is of order $\mathcal{O}(N/n)$. For example, if $N = 2000$ and $n = 7$, SVD-LPF is about 300 times more demanding than EKF. However, note that particle filters operations are highly parallelizable in practice, which may result in a significant computational time reduction when implemented for real-time applications [40]. Note also that the resampling step is not triggered at each time-step, which contributes to reducing the global computation time.

5.3.2. Real time implementation

The computational demand of the filters requires advanced real time processing capability, which is currently being developed for a number of space missions, such as GPU computing based real time operations at NASA's Goddard spaceflight centre for the Magnetospheric Multiscale (MMS) Mission [21].

The computation times of the particle filters used here represented slightly less than 10% of the simulation time in both cases. This setup can be considered for ground validations and comparison purposes, but more advanced specialised real time computation hardware, such as the abovementioned GPU approach, would be required for validation onboard a satellite. Further computational enhancements are possible by algorithmic improvements, such as the ability to vary and tune filter parameters including the numbers of particles, which can be reduced when estimation error covariances are low. This was however beyond the scope of this paper, where the focus is on robustness and estimation accuracy and their dependency on the availability and accuracy of measurements.

6. Conclusion

A gyroless satellite attitude determination approach using Sun sensors and magnetometers was proposed using a combined SVD and LPF approach. It is based on a Laplace approximation of the posterior density and feeding the LPF

with indirect attitude measurements through the SVD approach. A Procrustes problem formulation was successfully used to analytically solve Wahba's optimisation problem using Sun and magnetic field vector measurements and a third virtual predicted measurement that remained available during Sun occlusion. A Monte Carlo numerical simulation analysis confirms that the SVD-LPF filter significantly enhances accuracy compared to the regularized particle filter (RPF) when both types of sensor measurements are available and is significantly more accurate and robust to measurement discontinuities during solar eclipse under either coarse or fine magnetometer sensing. Compared to the RPF, the average roll, pitch and yaw RMSE results are reduced by factors of at least 4.44, 3.52 and 5.51, respectively, for the scenarios under consideration with moderate to high magnetometer accuracies. The SVD-LPF approach allows for the integration of more robust AOCS functionality in gyroless satellites. It can also yield cost reductions compared to more expensive sensing configurations with a similar performance. As part of the future work, we aim to combine the SVD-LPF with stochastic feedback attitude control to enforce probabilistic constraints under a high initial uncertainty.

Declaration of competing interest

The authors declare that they have no known competing financial interests or personal relationships that could have appeared to influence the work reported in this paper.

Appendix

Let $\mathcal{L}(q) = \mathbf{R}(q)\mathbf{B}_a$ where $\mathbf{R}(q)$ is defined on (8). The 1^{st} order Taylor expansion of the function $\mathcal{L}(q)$ around $\mathbf{q}_0$ is given by:

$$\begin{aligned} \mathbf{Y}_a &= \mathcal{L}(\mathbf{q}) \\ &\approx \mathcal{L}(\mathbf{q}_0) + \left.\frac{\partial \mathcal{L}}{\partial \mathbf{q}}\right|_{\mathbf{q}=\mathbf{q}_0} (\mathbf{q}-\mathbf{q}_0). \end{aligned} \tag{A.1}$$

The covariance matrix Σ of $\mathbf{Y}_a$ is approximated by:

$$\begin{aligned} \Sigma &\approx \mathbb{E}\left(\left.\frac{\partial \mathcal{L}}{\partial \mathbf{q}}\right|_{\mathbf{q}=\mathbf{q}_0} (\mathbf{q}-\mathbf{q}_0)(\mathbf{q}-\mathbf{q}_0)^T \left.\frac{\partial \mathcal{L}}{\partial \mathbf{q}}\right|_{\mathbf{q}=\mathbf{q}_0} \right) \\ &= \left.\frac{\partial \mathcal{L}}{\partial \mathbf{q}}\right|_{\mathbf{q}=\mathbf{q}_0} \mathbb{E}((\mathbf{q}-\mathbf{q}_0)(\mathbf{q}-\mathbf{q}_0)^T) \left.\frac{\partial \mathcal{L}}{\partial \mathbf{q}}\right|_{\mathbf{q}=\mathbf{q}_0} \\ &= \left.\frac{\partial \mathcal{L}}{\partial \mathbf{q}}\right|_{\mathbf{q}=\mathbf{q}_0} \mathbf{P}_{11}^{-} \left.\frac{\partial \mathcal{L}}{\partial \mathbf{q}}\right|_{\mathbf{q}=\mathbf{q}_0}. \end{aligned} \tag{A.2}$$

The function $\mathcal{L}(\mathbf{q})$ is given by:

$$\mathcal{L}(\mathbf{q}) = \mathbf{R}(\mathbf{q})\mathbf{B}_a = \begin{pmatrix} \mathcal{L}_{11}B_{a_1} + \mathcal{L}_{12}B_{a_2} + \mathcal{L}_{13}B_{a_3} \\ \mathcal{L}_{21}B_{a_1} + \mathcal{L}_{22}B_{a_2} + \mathcal{L}_{23}B_{a_3} \\ \mathcal{L}_{31}B_{a_1} + \mathcal{L}_{32}B_{a_2} + \mathcal{L}_{33}B_{a_3} \end{pmatrix} \triangleq \begin{pmatrix} l_1 \\ l_2 \\ l_3 \end{pmatrix}, \tag{A.3}$$

where $\mathbf{B}_a = [B_{a_1}, B_{a_2}, B_{a_3}]^T$.

The matrix $\frac{\partial \mathcal{L}}{\partial \mathbf{q}}$ can then be obtained as follows:

$$\frac{\partial \mathcal{L}}{\partial \mathbf{q}} = \begin{pmatrix} \frac{\partial l_1}{\partial q_0} & \frac{\partial l_2}{\partial q_0} & \frac{\partial l_3}{\partial q_0} \\ \frac{\partial l_1}{\partial q_1} & \frac{\partial l_2}{\partial q_1} & \frac{\partial l_3}{\partial q_1} \\ \frac{\partial l_1}{\partial q_2} & \frac{\partial l_2}{\partial q_2} & \frac{\partial l_3}{\partial q_2} \\ \frac{\partial l_1}{\partial q_3} & \frac{\partial l_2}{\partial q_3} & \frac{\partial l_3}{\partial q_3} \end{pmatrix}, \tag{A.4}$$

where:

$$\begin{cases} \dfrac{\partial l_1}{\partial q_0} = -2q_0B_{a_1} - 2q_1B_{a_2} + 2q_2B_{a_3} \\ \dfrac{\partial l_1}{\partial q_1} = 2q_1B_{a_1} - 2q_0B_{a_2} + 2q_3B_{a_3} \\ \dfrac{\partial l_1}{\partial q_2} = 2q_2B_{a_1} + 2q_3B_{a_2} + 2q_0B_{a_3} \\ \dfrac{\partial l_1}{\partial q_3} = -2q_3B_{a_1} + 2q_2B_{a_2} + 2q_1B_{a_3} \end{cases} \tag{A.5}$$

$$\begin{cases} \dfrac{\partial l_2}{\partial q_0} = 2q_1B_{a_1} - 2q_0B_{a_2} + 2q_3B_{a_3} \\ \dfrac{\partial l_2}{\partial q_1} = 2q_0B_{a_1} + 2q_1B_{a_2} - 2q_2B_{a_3} \\ \dfrac{\partial l_2}{\partial q_2} = 2q_3B_{a_1} - 2q_2B_{a_2} - 2q_1B_{a_3} \\ \dfrac{\partial l_2}{\partial q_3} = 2q_2B_{a_1} + 2q_3B_{a_2} + 2q_0B_{a_3} \end{cases} \tag{A.6}$$

$$\begin{cases} \dfrac{\partial l_3}{\partial q_0} = 2q_2 B_{a_1} + 2q_3 B_{a_2} + 2q_0 B_{a_3} \\ \dfrac{\partial l_3}{\partial q_1} = -2q_3 B_{a_1} + 2q_2 B_{a_2} + 2q_1 B_{a_3} \\ \dfrac{\partial l_3}{\partial q_2} = 2q_0 B_{a_1} + 2q_1 B_{a_2} - 2q_2 B_{a_3} \\ \dfrac{\partial l_3}{\partial q_3} = -2q_1 B_{a_1} + 2q_0 B_{a_2} - 2q_3 B_{a_3} \end{cases} \tag{A.7}$$

References

[1] A. D. Anderson, J. J. Sellers, Y. Hashida, Attitude determination and control system simulation and analysis for low-cost micro-satellites, in: Proceedings of the IEEE aerospace conference, Big Sky, Montana, Vol. 5, 2004, pp. 2934.

[2] V. V. Unhelkar, H. B. Hablani, Spacecraft attitude determination with Sun sensors, horizon sensors and gyros: Comparison of steady-state Kalman filter and extended Kalman filter, in: D. Choukroun, Y. Oshman, J. Thienel, M. Idan,(eds) Advances in estimation, navigation, and spacecraft Control. ENCS 2012, Springer, Berlin, Heidelberg, 2015, pp. 413-437.

[3] J. L. Crassidis and F. L. Markley, unscented filtering for spacecraft attitude estimation, Journal of Guidance, Control, and Dynamics, 26 (4)(Jul-Aug. 2003) 536-542.

[4] D. Cilden, E. S. Conguroglu, C. Hajiyev, Covariance analysis of three-axis attitude determination using two vector measurements, in: 7th International Conference on Recent Advances in Space Technologies (RAST), 2015.

[5] C. Hajiyev, D. C., Guler, Review on gyroless attitude determination methods for small satellites, Progress in Aerospace Sciences, 90 (2017) 54–66.

[6] A. R. Forbes, A. H. J. De Ruiter, Linear-matrix-inequality-based solution to Wahba's problem, Journal of Guidance, Control, and Dynamics, 38 (1), (Jan. 2015), 147-151.

[7] D. Modenini, Attitude Determination from Ellipsoid Observations: A Modified Orthogonal Procrustes Problem, Journal of Guidance, Control, and Dynamics, 41 (10), (Jun. 2018), 1-6.

[8] X-Y. Jiang, G-F. Ma, Spacecraft attitude estimation from vector measurements using particle filter, in: Proceedings of the Fourth International Conference on Machine Learning and Cybernetics, Guangzhou, August 2005.

[9] J. L. Crassidis, F. L. Markley, Y. Cheng, A survey of nonlinear attitude estimation methods, Journal of Guidance, Control, and Dynamics, 30 (1) (Jan-Feb. 2007) 12-28.

[10] N. J. Gordon, D. J. Salmond, A. F. M. Smith, Novel approach to nonlinear/non-Gaussian bayesian state estimation, Proceedings of the IEE, Part F, 140 (2) (1993) 107-113.

[11] M. S. Arulampalam, S. Maskell, N. Gordon and T. Clapp, Tutorial on particle filters for online nonlinear/non-Gaussian Bayesian tracking, IEEE Transactions on signal processing, Vol. 50, No. 2, 2002, pp. 174-188.

[12] M. Hürzeler and H. R. Künsch, Monte Carlo approximations for general state space models, Journal of Computational and graphical Statistics, 7 (2) (1998) 175-193.

[13] Ch. Musso, N. Oudjane, F. Legland, Improving regularized particle Filter, Sequential Monte-Carlo Methods in Practice, in: Doucet, A., de Freitas, N., Gordon, N. (eds), Sequential Monte Carlo Methods in Practice. Statistics for Engineering and Information Science. Springer, New York, NY, 2001, pp. 247-271.

[14] N. Merlinge, K. Dahia, H. Piet-Lahanier, J. Brusey, N. Horri, A box regularized particle filter for state estimation with severely ambiguous and nonlinear measurements, Automatica, 104 (2019) 102-110.

[15] P. Wang, L. Mihaylova, P. Bonnifait, P. Xu, J. Jiang, Feature-refined box particle filtering for autonomous vehicle localisation with OpenStreetMap. Engineering Applications of Artificial Intelligence, 105 (2021) 104445.

[16] C. Musso, P. B. Quang, F. Le Gland, Introducing the Laplace approximation in particle filtering, in: 14th International Conference on Information Fusion, Chicago, Illinois, USA, July 5-8, 2011.

[17] C. Musso, P. B. Quang, and A. Murangira, A Laplace-based particle filter for track-before-detect, in: 18th IEEE International Conference on Information Fusion (Fusion), 2015, pp. 1657-1663.

[18] P. B. Quang, C. Musso, F. Le Gland, Particle filtering and the laplace method for target tracking, IEEE Transactions on Aerospace and Electronic Systems, 52 (1), 2016.

[19] C. Musso, B. Sacleux, A. Bresson, J.-M. Allard, K. Dahia, Y. Bidel, N. Zahzam, C. Palmier, Terrain-aided navigation with an atomic gravimeter, in: 22nd International Conference on Information Fusion (FUSION), Ottawa, Canada, 2019.

[20] Y. Yafei, L. Jianguo, Particle filtering for gyroless attitude/angular rate estimation algorithm, in: First International Conference on Pervasive Computing, Signal Processing and Applications, 2010, pp. 1188-1191.

[21] A. Brown and J. Tichy and M. Demoret and D. Rand, GPU Accelerated Conjunction Assessment with applications to formation flight and space debris tracking, in: Astrodynamics Specialist Conference (ASC) Hilton Head, 2013.

[22] G. Hendeby, J. Hol, R. Karlsson, and F. Gustafsson, A graphics processing unit implementation of the particle filter, in: Proceedings of the 15th European Statistical Signal Processing Conference, Poznan, Poland, September 2007, pp. 1639-1-71643.

[23] X.-Y. Jiang and G.-F. Ma, Spacecraft attitude estimation from vector measurements using particle filter, in: Proceedings of the Fourth International Conference on Machine Learning and Cybernetics, Guangzhou, China, August 2005, pp. 682-687 Vol. 2.

[24] D. A. Vallado and W. D. McClain, Fundamentals of astrodynamics and applications, Microcosm Press, 2nd edition, 2001.

[25] M. D. Shuster and S. D. Oh, Three-Axis Attitude Determination from Vector Observations, Journal of Guidance and Control, Vol. 4, No. 1, 1981, pp. 70-77.

[26] M. D. Shuster, Maximum Likelihood Estimation of Spacecraft Attitude, Journal of the Astronautical Sciences, Vol. 37 , No. 1, 1989, pp. 79-88.

[27] M. D. Shuster, Kalman Filtering of Spacecraft Attitude and the QUEST Model, Journal of the Astronautical Sciences, Vol.38 , No. 3, 1990, pp. 377-393.

[28] Y. Cheng, J. L. Crassidis and F. L. Markley, Attitude estimation for large field-of-view sensors, The Journal of the Astronautical Sciences, 54, 433-448 (2006).

[29] F. L. Markley, Attitude Estimation or Quaternion Estimation? Journal of the Astronautical Sciences, Vol. 52, No 1/2, 2004, pp. 221-238.

[30] F. L. Markley, J. L. Cassidis and Y. Cheng, Nonlinear Attitude Filtering Methods, AIAA Guidance Navigation and Control Conference 2005-5927, 15-18 August 2005.

[31] P. H. Schönemann, A generalized solution of the orthogonal procrustes problem, Psychometrika, 31 (1966) 1–10.

[32] N. Ohta and K. Kanatani, Optimal estimation of three-dimensional rotation and reliability evaluation, in IEICE TRANSACTIONS on Information and Systems, 1998, pp. 1247-1252.

[33] L. Dorst, First order error propagation of the procrustes method for 3D attitude estimation, in: IEEE transactions on pattern analysis and machine intelligence, 2005, pp. 221-229.

[34] I. Söderkvist and P. Wedin, On condition numbers and algorithms for determining a rigid body movement, in: BIT Numerical Mathematics, 1994, pp. 424-436.

[35] A. Doucet and A. M. Johansen, A Tutorial on Particle Filtering and Smoothing: Fifteen Years Later. In: D. Crisan and B. Rozovsky (eds.), Nonlinear Filtering Handbook, 2011, pp. 656-704. Oxford University Press, Oxford.

[36] S. W. Shepperd, Quaternion from Rotation Matrix, J. Guidance, Vol. 1, No. 3, May-June, 1978, pp. 223-224.

[37] M. J. Hale, P. Vergez, M. J. Meerman and Y. Hashida, Kalman filtering and the attitude determination and control task. AIAA-2004-6018, USAFA, Department of Astronautics, USAF Academy CO 80840, 2004.

[38] R. Karlsson, T. Shon and F. Gustafsson, Complexity analysis of the marginalized particle filter, in: IEEE Transactions on Signal Processing, Vol. 53, No. 11, 2005, pp. 4408-4411.

[39] M. Verhaegen and P. V. Dooren. Numerical aspects of different Kalman filter implementations. In: IEEE Transactions on Automatic Control 31.10 (1986), pp. 907–917.

[40] N. Merlinge, C. Audebert, K. Dahia, B. Hérissé and J.-M. Allard, Particle filtering method and navigation system using measurement correlation. U.S. Patent Application No. 17/612, 753.